#### **ORIGINAL ARTICLE**



# Simulations of modulated plane waves using weakly compressible smoothed particle hydrodynamics

Samarpan Chakraborty<sup>1</sup> · Kayo Ide<sup>2</sup> · Balakumar Balachandran<sup>3</sup>

Received: 23 April 2023 / Accepted: 31 August 2023 / Published online: 27 September 2023 © The Author(s), under exclusive licence to Springer-Verlag London Ltd., part of Springer Nature 2023

#### Abstract

Extreme waves, also known as 'rogue waves', have posed considerable challenges to maritime traffic over some time. Efforts have been directed at investigating the mechanisms governing these extreme energy localizations in oceanic environments. Modulational instability, also known as sideband instability, is one such mechanism that has been proposed to explain the occurrence of such phenomena in the framework of non-linear theory. The current work is aimed at better understanding the effects of sideband modulations on the propagation of unidirectional waves. To achieve this, a numerical wave tank (NWT) has been constructed using Weakly Compressible Smoothed Particle Hydrodynamics (WCSPH) to investigate the different parameters associated with the generation and propagation of plane, modulated waves. General Process Graphics Computing Unit (GPGPU) computing has been utilized to accelerate the computational process and improve the computational efficiency. The chosen numerical scheme has been validated by carrying out irregular waves focusing simulations to compare with available experimental data. Additionally, a Peregrine-type breather experiment has also been performed as part of the validation studies to look at energy localization within the NWT. The effects of the different parameters associated with the modulations to a plane propagating wave have been investigated using a blend of surface elevation data, eigenvalue, and frequency spectra. The effect of water depth on the perturbations to plane waves has been also investigated. The observations from these experiments can help shed light into the effects of modulations in the propagation of plane waves and help in the study of oceanic energy localization studies in future.

 $\textbf{Keywords} \ \ WCSPH \cdot GPGPU \cdot Modulational \ instability \cdot Numerical \ simulations \cdot Numerical \ wave \ tank$ 

- Balakumar Balachandran balab@umd.edu
  - Samarpan Chakraborty schakr18@umd.edu

Kayo Ide ide@umd.edu

- Computational Dynamics Laboratory, Department of Mechanical Engineering, University of Maryland, College Park, MD 20742, USA
- Department of Atmospheric and Oceanic Science, Department of Mathematics, Earth System Science Interdisciplinary Center, Institute of Physical Science and Technology, University of Maryland, College Park, MD 20742, USA
- Department of Mechanical Engineering, University of Maryland, College Park, MD 20742, USA

#### 1 Introduction

Extreme oceanic waves [2], more popularly known as 'rogue waves', are large-amplitude waves that appear suddenly on the ocean surface and tend to disappear without a trace [3]. Such extreme energy localizations can have a devastating impact on maritime traffic and offshore operations. Considerable research efforts have been directed at the investigation and prediction of such occurrences. Several mechanisms have been proposed to explain this phenomenon in different oceanic scenarios [17, 21]. A general review of different physical mechanisms governing the formation of rogue waves was provided by Pelinovsky and Kharif [33]. Linear mechanisms include superposition of different monochromatic wave components via geometric focusing [20]. The effect of linear directional focusing behind such phenomena was investigated by Adcock et al. [1] through numerical modeling of the widely studied Draupner Wave [6]. The modification of the linear focusing due to the introduction



of non-linearity via phase modulation has been investigated by Wang and Balachandran [36]. Atmospheric forcing and wave-current interactions [39] have also been observed to lead to such high waves. The phenomenon of modulational instability ("Modulational Instability and Rogue Waves in Crossing Sea States in: Journal of Physical Oceanography Volume 48 Issue 6 (2018)," n.d.) is another phenomenon that has been theoretically proposed in the framework of weakly non-linear theory to explain the formation of such extreme energy localizations.

The phenomenon of modulational instability has been observed in a wide variety of non-linear physical systems, ranging from plasma waves [19], electromagnetic beams to water waves [37]. In the framework of the analysis of sudden extreme energy localizations in oceanic environments, this is more commonly known as the Benjamin-Feir (BF) instability [18]. The effect of this phenomenon results from the interaction between a strong carrier wave and perturbations in the form of lower and higher frequency sidebands, resulting in instabilities due to exponential growth spatiotemporally.

Numerous studies have been conducted to investigate the mechanism of modulational instability in oceanic waves. Wave tank experiments were performed by Onorato et al. [32] and subsequent statistical and probability analyses were performed to explain the observations in terms of the modulational instability mechanism. Numerical modeling using full non-linear equations was used by Chalikov [13] for investigation of the growth of the BF instability in an initially homogeneous Stokes wave train. Water wave experiments exhibiting non-linear modulation have been discussed in Bonnefoy et al. [10] through numerical tools of non-linear spectral analysis. Numerical wave tank experiments provide an excellent alternative to physical models in offshore and coastal engineering situations in regard to resources and scale efforts, thus allowing for improved opportunities to carry out investigations for extreme energy localizations in oceanic environments.

Different numerical models can be utilized for simulations of wave tank studies depending on the size and complexity of the simulation domain or resolution, among other factors. Weakly Compressible Smoothed Particle Hydrodynamics (WCSPH) [28] is a Lagrangian method that has been used quite extensively in the last few decades for simulation of astrophysical phenomena and wave tank studies. Longcrested wave generation studies using WCSPH were carried out by Altomare et al. [4] to validate against theoretical and experimental observations. Different numerical dissipation schemes and kernel functions were investigated for effectiveness in numerical wave tank simulations by the authors in a prior study [12]. Energy localization studies due to current gradients in ocean waves were carried out by Manolidis et al. [23]. New rogue wave forms were studied by Chabalko et al.

[11] and Moitra et al. [26] by utilizing the massive parallelization inherent in GPU computing.

Numerical modeling of fluids can be implemented through two broad approaches in SPH literature. Incompressible Smoothed Particle Hydrodynamics (ISPH) [22], as the name suggests, is based on enforcing a very low level of compressibility of the fluid through solution of a pressure Poisson equation. Although the method is accurate, it involves substantial computational time and resources, which might not be relevant for large scale numerical experiments. The Weakly Compressible Smoothed Particle Hydrodynamics, on the other hand, is based on a weakly compressible fluid assumption and solved using a stiff equation of state. Diego and Colagrossi [15] showed that free surface motion can be intrinsically tracked using WCSPH in hydrodynamic simulations. This is utilized in numerical wave tank simulations for an efficient and accurate recording of free surface elevation.

The authors' aim in the current work is to investigate the influence of modulation in unidirectional waves traveling in an NWT through simulations of perturbed plane waves using different sets of parameters through a WCSPH scheme. The study is closely based on the work carried out by Eeltink et al. [16] investigating the non-linear evolution of waves in experimental wave tanks followed by subsequent predictions using deep learning frameworks. An overview of the basic concepts used in this study of plane perturbed waves is provided in Fig. 1. As the initial effort, an NWT has been constructed using a WCSPH numerical scheme. Using this setup, several simulations have been conducted by variation of the different parameters involved in the wave making. The surface elevation measurements from these experiments have been then utilized for carrying out different analyses. The observations from these efforts are aimed at examining the influence of perturbation sidebands and particularly their asymmetry, as well as investigating the effect of the modulation frequency and water depth d. The steps involved in this workflow will be explored later in a more detailed manner. With that in mind, the rest of the paper is organized as follows. Firstly, in the next section, the authors provide a brief description of the WCSPH formulation used along with the different analysis techniques being utilized for the studies on perturbed plane waves. Following this, irregular wave focusing experiments are simulated using available wave conditions for the validation of the scheme used in the numerical model. The evolution of a modulated wave group in the NWT, described using a Peregrine type breather solution has also been discussed in the Appendix as part of our validation studies for the numerical scheme. Subsequently, in the following section, parametric studies on modulated waves have been conducted using the workflow as discussed in Fig. 1. Finally, the conclusions are drawn based upon the observations to provide insight into the wave evolution



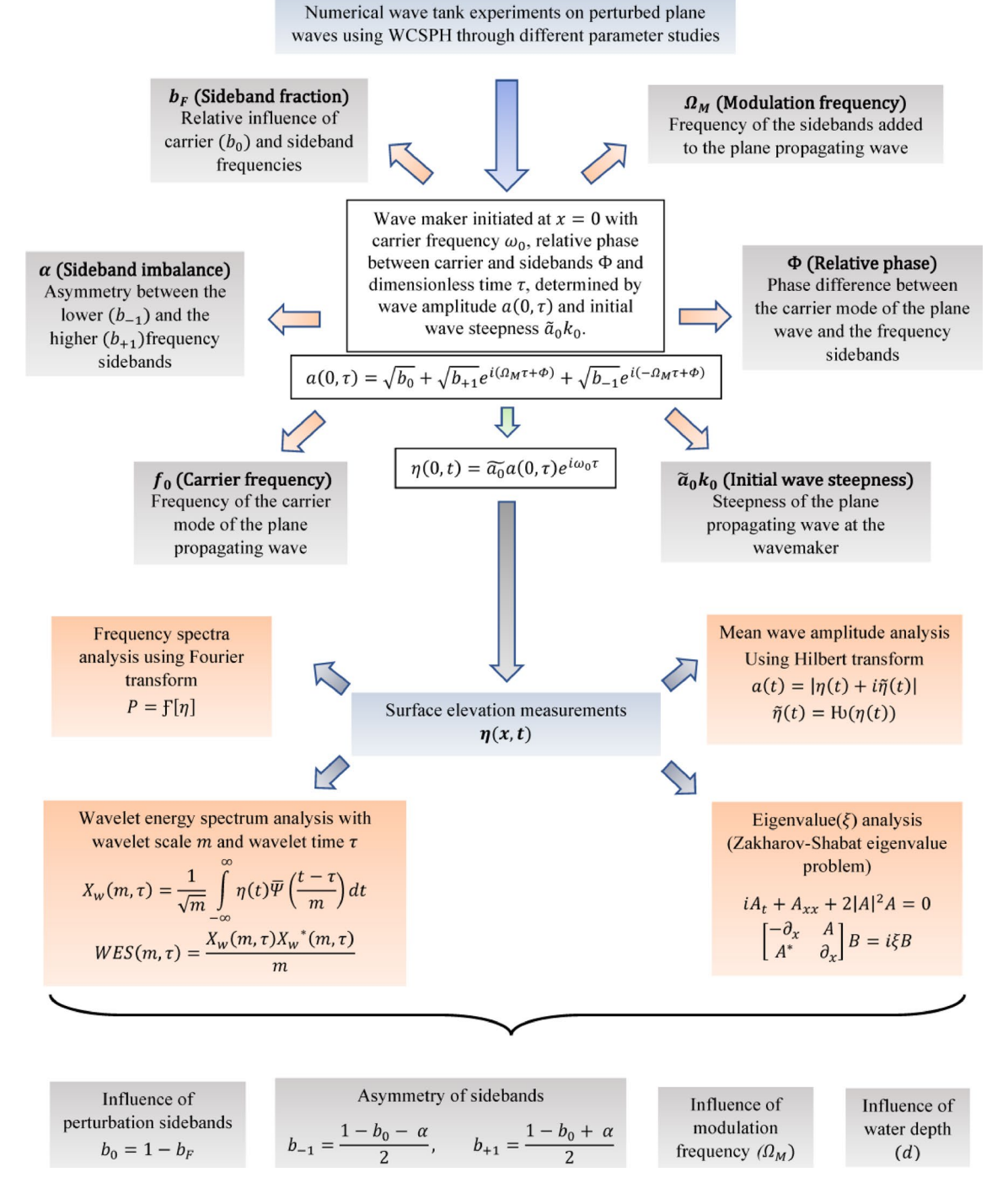


**Fig. 1** An overview of the basic concepts used in this study of plane perturbed waves in numerical wave tanks. A numerical wave tank has been constructed using the WCSPH scheme. Different experiments have been carried out on plane perturbed waves using this developed numerical model. The surface elevation measurements from these

experiments have been utilized for carrying out different analyses. The observations from these efforts are aimed at examining the influence of perturbation sidebands and particularly their asymmetry, as well as investigating the effect of the modulation frequency and relation to water depth

due to modulations in plane wave propagation scenarios. The authors are hopeful that the results from this work can help in energy localization studies in oceans that the authors intend to carry out in future.

#### 2 Methods

The WCSPH scheme implemented in this paper is closely based upon the work of Monaghan [28]. It is based on the



Navier–Stokes equation where fluid properties are described primarily through density and momentum equations as given in Eqns. 2 and 5 using a smoothing function  $W(r_{ij},h)$  which takes into account the contribution of neighboring particles for fluid property calculation at a particular position. The different function values at any particular computational node i is computed using the discretized SPH equation of the form

$$q_i(r) = \sum_{i} q_j \frac{m_j}{\rho_j} W(r_i - r_j, h)$$
(1)

where  $q_j$  is the function value at the  $j^{th}$  point,  $W(r_{ij}, h)$  is a smoothing function,  $m_j$  and  $\rho_j$  are the mass and density related to the  $j^{th}$  particle and h is the smoothing length for  $W(r_{ij}, h)$ . The particle masses in this work are assumed to be constant and are represented by  $m_i$ . The particle densities  $\rho_i$  can be computed accordingly as

$$\rho_i = \sum_j m_j \ W(r_{ij}, h) \tag{2}$$

Following this, the particle pressures  $P_i$  can be computed using a stiff equation of state proposed by Batchelor [7] as:

$$P = B\left(\left(\frac{\rho}{\rho_0}\right)^{\gamma} - 1\right) \tag{3}$$

where  $\gamma=7$ ,  $\rho$  is the current density of the particle and  $\rho_0$  is the reference density. The constant B, termed as bulk modulus gives a measure of the incompressibility of the medium and the relative density fluctuations during the simulations. It depends on the anticipated maximum velocity of the fluid  $V_f$  and a chosen compressibility factor  $\eta$  and is given by

$$B = \frac{\rho_0 c_s^2}{\gamma} \tag{4}$$

where  $c_s = \frac{V_f}{\sqrt{\eta}}$ . The Navier–Stokes equation for the Lagrangian formulation is then used for computing the particle accelerations as

$$\frac{dv_i}{dt} = -\sum_i m_j \left(\frac{P_i}{\rho_i^2} + \frac{P_j}{\rho_j^2}\right) \nabla_i W(r_{ij}, h) + V_{Ti} + F_i$$
 (5)

where  $\nabla_i W(r_{ij}, h)$  represents the kernel gradient function,  $V_{Ti}$  represents the acceleration due to viscous forces and  $F_i$  gives the acceleration due to body forces. The rate of change of density of the particles  $\frac{d\rho_i}{dt}$  are computed as follows:

$$\frac{d\rho_i}{dt} = \sum_j m_j v_{ij} \cdot \nabla_i W(r_{ij}, h)$$
 (6)

Finally, the particles are moved forward in time by calculating their velocities  $v_i$  and positions  $r_i$  from their respective

accelerations  $a_i$  using a modified version of the conventional leap-frog formulation.

$$v_{i+\frac{1}{2}} = v_{i-\frac{1}{2}} + a_i dt \tag{7a}$$

$$v_{i+1} = v_{i+\frac{1}{2}} + a_i \frac{dt}{2} \tag{7b}$$

$$r_{i+1} = r_i + v_{i+\frac{1}{2}}dt \tag{8}$$

The weakly compressible nature of the WCSPH approach makes it susceptible to spurious density fluctuations during simulations. Computation of the viscous term in the NS equation involves calculation of the Laplacian of the smoothing function, and this can lead to instabilities in the numerical scheme. Introduction of numerical dissipation thus plays a key role in this numerical scheme to help dissipate the unwanted pressure oscillations. Different dissipation schemes like the artificial viscosity, density reinitialization and the  $\delta$ -SPH scheme have been proposed in the SPH literature over the years [5, 15, 27]. The effectiveness of the different dissipation schemes in carrying out numerical wave tank simulations was investigated in a prior study carried out by the authors [12]. Using the results from the study, a dissipation scheme was chosen by implementing the parameters  $\beta$  and  $\delta$  in the viscous force term  $V_{Ti}$  and the density change rate  $\frac{d\rho_i}{dt}$  respectively as

$$V_{Ti} = \begin{cases} V_{Ti}^{Mor} - m_j \frac{\rho \mu_{ij}^2}{\rho_{ij}} \nabla_i W(r_{ij}, h), v_{ij}, r_{ij} < 0 \\ V_{Ti}^{Mor}, v_{ij}, r_{ij} > 0 \end{cases}$$
(9)

where  $\mu_{ij} = \frac{h v_{ij} \cdot r_{ij}}{r_{ij}^2}$ ,  $\overline{\rho_{ij}} = \frac{\rho_i + \rho_j}{2}$  is the density average of the  $i^{th}$  and the  $j^{th}$  particles.  $V_{Ti}^{Mor}$  is the viscosity term implemented by Morris et al. [30] and is given by  $V_{Ti}^{Mor} = \sum_j \frac{m_j (\mu_i + \mu_j)}{\rho_i \rho_j} \left( \frac{1}{|r_{ij}|} \frac{\partial W_{ij}}{\partial r_i} \right)$ . The parameter  $\beta$  is used to prevent unphysical particle penetration and helps achieve numerical stability.

The  $\delta$  dissipation term added to the rate of change density equation reads as

$$\frac{d\rho_i}{dt} = \sum_i m_j v_{ij} . \nabla_i W(r_{ij}, h) + D_a$$
 (10)

where  $D_a$  encompasses the dissipation term in the form

$$D_a = 2\delta h c_0 \sum_j \frac{m_j}{\rho_j} \psi_{ji} \frac{(r_j - r_i) \cdot \nabla_i W_{ij}}{(r_i - r_i)^2}$$
(11)

Here,  $\psi_{ji}$  is a second-order term implemented in the form  $\psi_{ii} = \rho_i - \rho_i$  in the present study.

The smoothing kernel functions used in WCSPH also play a prominent role in the modeling as pointed out by Dehnen and



Aly [14]. The efficacy of kernel functions in conjunction with a suitable numerical dissipation scheme in wave tank was also examined in the prior work carried out by the authors [12]. Following the observations from that study, the fifth degree Wendland class 2 kernel W(r,h) has been used for the numerical simulations performed in this work. The domain radius has been taken as 2h for this chosen kernel function, where h is the smoothing radius. In all the simulations performed in the current work, h has been taken to be  $1.5\Delta x$ , where  $\Delta x$  is the fluid particle spacing. The kernel function and its derivative are given as:

$$W(r,h) = \begin{cases} \frac{7}{4\pi h^2} (2z+1) \left(1 - \frac{z}{2}\right)^4, \ 0 \le z \le 2\\ 0, \qquad z > 2 \end{cases}$$
 (12)

$$\nabla W(r,h) = \begin{cases} -\frac{35}{4\pi h^3} \left(1 - \frac{z}{2}\right)^3 z \frac{r}{|r|}, \ 0 \le z \le 2\\ 0, \qquad z > 2 \end{cases}$$
 (13)

Here,  $z = \frac{|r|}{h}$ , where *r* is the distance from the considered particle to its neighboring particles.

Dynamic boundary conditions have been implemented for the domain boundaries in all the numerical experiments carried out in this study. The same set of equations applies for the boundary particles too, with the only constraint being their motion is governed by externally applied forces. This reduces the computational effort associated with the numerical modelling. The numerical model thus described has been run using CUDA 11.7.0 ("NVIDIA CUDA Toolkit Release Notes," n.d.) to utilize its massively parallel computational nature. In addition, the process has been accelerated by making use of the powerful p100 GPU partition available via the high-performance computing (HPC) facilities of the Bluecrab ("Bluecrab HPC Cluster," n.d.) cluster and the a100 GPU partition available via the HPC facilities of the Zaratan cluster [38], allowing for substantially reduced computational times.

The plane modulated waves generated in our simulations involve a carrier wave perturbed with two frequency sidebands, where the resultant wave amplitude is expressed as follows.

$$a(0,\tau) = \sqrt{b_0} + \sqrt{b_{+1}} e^{i(\Omega_M \tau + \Phi)} + \sqrt{b_{-1}} e^{i(-\Omega_M \tau + \Phi)}$$
 (14)

(14) Here,  $\sqrt{b_0}$ ,  $\sqrt{b_{-1}}$  and  $\sqrt{b_{+1}}$  are the amplitudes of the carrier mode and the two frequency sidebands, respectively. The amplitudes are determined using the parameters  $b_F$  and  $\alpha$  using the equations

$$b_0 = 1 - b_F, b_{-1} = \frac{1 - b_0 - \alpha}{2}, b_{+1} = \frac{1 - b_0 + \alpha}{2} \tag{15} \label{eq:15}$$

where  $b_F$  is the sideband fraction and  $\alpha$  can be termed as sideband imbalance.  $\Omega_M$  in Eq. 14 is the modulation frequency of the sidebands,  $\Phi$  gives the relative phase between the sidebands and the carrier mode and  $\tau$  is the

dimensionless time. The piston maker displacement can be constructed using the surface elevation at x = 0 given by

$$\eta(0,t) = \widetilde{a}_0 a(0,\tau) e^{i\omega_0 t} \tag{16}$$

where  $\widetilde{a_0}$  is the initial value of the non-dimensional amplitude. The readers are encouraged to look at the original paper [16] for a detailed explanation of the non-dimensionalization of the different quantities.

For the different validation and perturbed wave studies, the surface elevation readings  $\eta(t)$  are obtained at the different wave gauge locations following the NWT experiments. These measurements are then analyzed using different approaches to look at the influence of the different parameters involved as depicted in Fig. 1. The frequency spectra over the wave tank, found out using the Fourier transform gives an account of the energy in the different frequency bands as the wave propagates through the NWT. This helps visualize the relative influence of the carrier and the frequency sidebands during the wave propagation process. Apart from this approach, the wave amplitudes at the different wave gauge locations over the time of propagation are calculated using the Hilbert transform according to the given formula as follows.

$$a(t) = \left| \eta(t) + i\widetilde{\eta}(t) \right| \tag{17}$$

where  $\tilde{\eta}(t) = H(\eta(t))$  and  $H(\eta) = F^{-1}[-i \ sign(\omega)]$   $F[\eta]]$  where F is a Fourier transform and  $\omega$  is the angular frequency. For the current study  $(\eta(t))$  has been computed using the 'hilbert' function in MATLAB. The time average of these wave amplitudes is then computed at the different wave gauge locations to further provide information about the energy propagation over the wave tank for the different sets of parameters.

In contrast to these approaches, the wavelet energy spectrum method helps understand the energy variations in the different frequency bands at different time instants over the simulation duration. This helps understand the time–frequency relationship inherent in the surface elevation time series at different locations along the NWT. The analytical Morlet wavelet ("Morlet wavelet—MATLAB Morlet," n.d.) used as the mother wavelet for this analysis can be defined in the frequency domain as:

$$\widehat{\Psi}(\omega) = 2e^{-\frac{(\omega - 6)^2}{2}}\widehat{U}(\omega) \tag{18}$$

Using the inverse Fourier transform, the Morlet wavelet in the time domain can be expressed as:

$$\Psi(t) = \sqrt{\frac{2}{\pi}} e^{-\frac{t^2}{2} + 6it} \tag{19}$$

Using this, the continuous wavelet transform can be defined as:



$$X_{w}(m,\tau) = \frac{1}{\sqrt{m}} \int_{-\infty}^{\infty} \eta(t) \overline{\Psi}\left(\frac{t-\tau}{m}\right) dt$$
 (20)

where m is the wavelet scale and  $\tau$  is the wavelet time for time-frequency analysis and  $\eta(t)$  is the surface elevation time series. Following this, the wavelet energy spectrum can be computed as:

$$WES(m,\tau) = \frac{X_w(m,\tau)X_w^*(m,\tau)}{m}$$
 (21)

Finally, as part of our analysis process, the time histories of the surface elevation observations have been used to carry out eigenvalue analysis using a Zakharov-Shabat [37] eigenvalue system which can be defined as follows.

$$B_{x} = \begin{bmatrix} -i\xi & A \\ -A^{*} & i\xi \end{bmatrix} B \tag{22}$$

Here  $B(x, t, \xi)$  is a vector function,  $\xi$  is a spectral parameter and A is the non-dimensional wave amplitude defined in the non-dimensional NLS equation given by:

$$iA_t + A_{xx} + 2|A|^2 A = 0 (23)$$

The eigenvalue system can be written as a system of linear equations as follows.

$$\begin{bmatrix} -\partial_x & A \\ A^* & \partial_x \end{bmatrix} B = i\xi B \tag{24}$$

The Fourier collocation method was then used to break down this system into a discretized eigenvalue system to solve for the eigenvalues corresponding to the Fourier coefficients of the eigenfunction *B*.

#### 3 Results and discussion

#### 3.1 Validation studies

In a previous aforementioned study [12], the authors carried out numerical simulations of sloshing and wave tank experiments for validation of the WCSPH numerical scheme. In the present study, the chosen numerical dissipation scheme and the kernel function of the model has been validated for the study of modulated plane waves through simulations involving focusing of double wave groups in a NWT, the details of which experiments are available in the work by Wang et al. [35]. The surface elevation readings are obtained at various locations along the numerical wave tank and compared with the experimental observations. In addition to this, the developed numerical scheme has also been utilized to look at the phenomenon of modulation growth in a wave tank. The experimental setup outlined in Shemer and Alperovich (2013) has been used to carry out simulations of a Peregrine-type breather in a NWT. The surface elevation observations at the different locations are then used for analysis of the modulation growth. The simulation setup description and the corresponding discussions on this effort are provided in the Appendix.

The wave focusing experiments detailed out in Wang et al. [35] consists of a 69.0m long, 2.0m wide and 1.8m deep experimental wave flume with a water depth of d=1.2m. A piston maker is equipped at the left side of the flume for wave making and a wave absorbing zone is set up towards the end of the tank for wave absorbing arrangements. 25 wave gauges are set up for recording the surface elevations at desired locations. For the two-dimensional numerical wave tank simulations conducted in this study, a wave tank of length 81.2m and a height of 3.6m with a water depth of d=1.2m has been used. A piston wavemaker of length 2.4m is arranged towards the left part of the wave flume and a sloping beach extending from 49.7m to 81.2m is provided for passive wave absorption.

For purposes of comparison, 5 wave gauges (WGs) are set up in this wave flume at locations where the elevation readings are available in Wang et al.[35]. An illustration of the experimental setup is provided in Fig. 2. The fluid properties and the parameters used during the simulations are summarized in Table 1. The low values of the Courant number ensure that the scheme is numerically stable for all fluid particle resolutions.

The numerical experiments have been run using different fluid particle resolutions for a particular case of focusing of double wave groups. The wave parameters are given in Table 2.

Here,  $f_{p1}$  and  $f_{p2}$  are the peak frequencies associated with two different wave groups that are propagating in the same

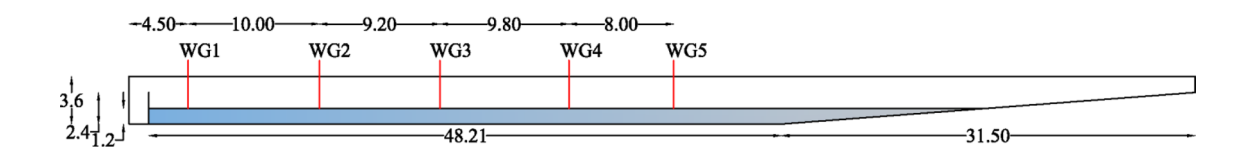


Fig. 2 Numerical setup for the irregular wave focusing experiments. All dimensions are provided in meters. The wave gauges are depicted using WG



Table 1 The simulation parameters in the WCSPH numerical setting used for the validation study on focusing experiments of the double wave groups

$\Delta x$	Fluid particle resolution	$\in \{3 \times 10^{-2} m, 4.5 \times 10^{-2} m, 6 \times 10^{-2} m, 9 \times 10^{-2} m, 12 \times 10^{-2} m\}$
	Courant number	∈ [0.00025, 0.001]
	Boundary particle resolution	$0.5 \Delta x$
h	Smoothing length	$1.5\Delta x$
β	Parameter for numerical stability	$\in [2.0, 4.0]$
δ	$\delta$ – SPH coefficient	0.001
$\rho_0$	Reference density	1000
$V_{max}$	Maximum fluid velocity	3.0m/s
$c_0$	Numerical speed of sound	$10v_{max}$
dt	Time step size	$1 \times 10^{-5}$ s
v	Morris' viscosity factor	$1 \times 10^{-6}$

Table 2 The wave parameters for the particular double wave group focusing case used for the validation study

$f_{p1}(Hz)$	$f_{p2}(Hz)$	$\Delta f_p(Hz)$	$A_b(cm) (f_{p1})$	$A_b(cm) (f_{p2})$	$x_b(m)$
0.8	0.7	0.1	4.32	4.39	22.2

direction in the wave tank.  $A_b$  denotes the focusing amplitude of an individual wave group while  $x_b$  gives the focusing position along the wave tank. The readers are directed to Wang et al. [35] for a detailed explanation of the procedure for determination of the individual frequencies and amplitudes of the wave components in each wave group. Following this work, the wave spectra for the two wave groups are discretized in the frequency range (0.4-2.0)Hz with each having the same  $N_f=200$  components. The displacement of the piston wavemaker X(t) is determined by superimposing the displacements for the individual wave groups using the equations for the free surface elevation  $\eta(t)$  and the transfer function  $T_{ki}$  for a piston-type wavemaker given as following.

$$\frac{\partial X(t)}{\partial t} = \sum_{i=1}^{N_f} \frac{\omega_i}{T_{ki}} a_i \cos\left[k_i \left(x - x_b\right) - 2\pi f_i \left(t - t_b\right)\right]$$
 (25)

Here, $a_i$  and  $f_i$  are the amplitude and frequency of a single wave component,  $t_b$  is the time of focusing while  $T_{ki}$  is the Biesel transfer function [8] for a piston type wavemaker given as follows.

$$T_{ki} = \frac{2\left[\cosh(2k_i d) - 1\right]}{2k_i d + \sinh(2k_i d)}$$
(26)

where d is the water depth in the numerical wave tank.

Free surface elevation readings are obtained at the different gauge locations for all the simulations to compare with the experimental readings available in Wang et al.[35]. The comparisons at x = 3m and x = 13m for a fluid particle resolution of  $\Delta x = 0.03m$  are presented in Figs. 3 and 4.

Additionally, the surface elevation time series  $\eta(t)$  have been used for analysis of the time–frequency relationship using the wavelet energy spectrum method as outlined in §2. For all the numerical experiments carried out in this study, the wavelet energy spectrum has been computed using the built-in 'cwt' function using the analytical 'amor' wavelet function in MATLAB ("MATLAB—MathWorks," n.d.).

As can be seen from the upper plot in Fig. 3, for the comparisons at x = 3m, the numerical surface elevation observations show considerable agreement with the experimental readings from t = 38s to t = 45s, when the two wave groups are in the process of focusing. The wave amplitude during this time duration is more than 2cm, while it is much lower during the initial times. As can be seen from the plot, there is reduced agreement between the experimental and the numerical results before t = 35s, where the amplitude is significantly lower than 2cm. This disagreement can be attributed to the numerical dissipation associated with WCSPH. As mentioned previously, numerical dissipation is essential for stability during the simulations, but its incorporation does not allow the complete development of the low amplitude waves observed initially. However, the purpose of the validation study was to investigate if the model can capture the energy focusing during the simulation. Though there are discernible differences between the two sets of readings, the model was able to correctly capture the focusing phenomenon at this location with respect to magnitude and phase. A wavelet energy spectrum for this time series has been shown in the lower plot in Fig. 3 to better capture the focusing process. The onset of energy localization between 40 and 45 s in the frequency range of 0.7 and 0.8 Hz can be clearly observed in this plot. A similar set of comparisons carried out for the wave gauge location at x = 13m is presented in Fig. 4. The surface elevation comparisons in the upper plot of Fig. 4 reveal a qualitative agreement with respect to the focusing phenomenon. However, there are discernible differences in the phase and magnitude of the elevation readings, where the magnitude of the focused wave group for the simulation is lower than the experimental observations. As in



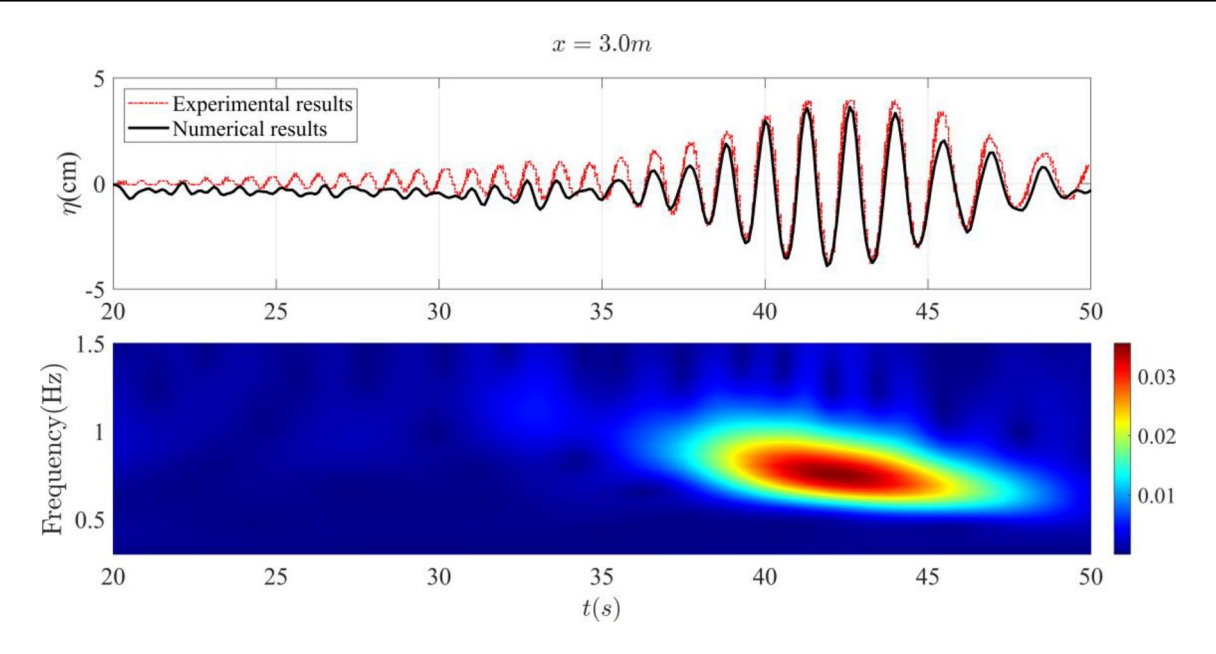


Fig. 3 Results of the validation study for  $\Delta x = 0.03$ m at x = 3m. The upper plot reveals the surface elevation comparisons between the numerical observations in this study and the experimental readings in

Wang et al. The lower plot gives the WES distribution for the surface elevation readings

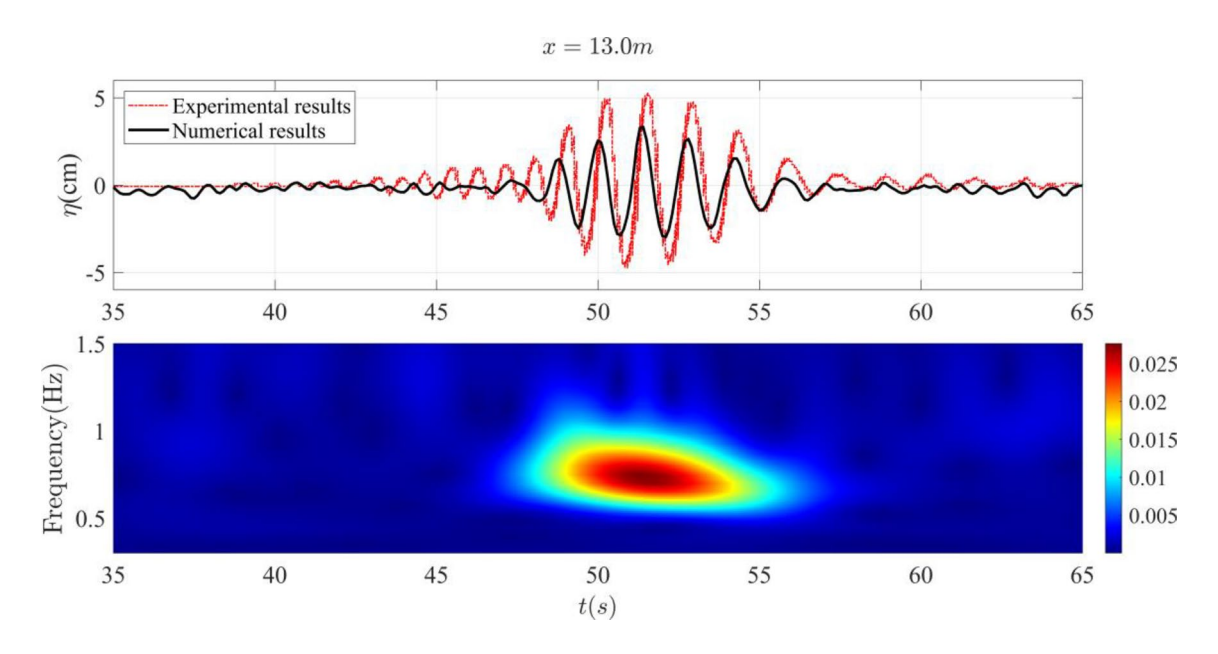


Fig. 4 Results of the validation study at x = 13 m similar to the depiction in Fig. 3

the previous case, these differences can be attributed to the dissipative effects of our numerical model, which increase with larger wave propagation distances. Despite these differences, the model was able to capture the focusing at this location which can be seen from the ratio of the focused wave packet with the background wave. This can be further examined using the wavelet transform plot at this location represented in the lower plot of Fig. 4. The WES plot reveals that the focusing takes place over a narrower time range and

starts encompassing more frequencies as compared to the observations at x = 3m, signifying the growth of the focusing phenomenon. Thus, it can be discerned from the results of this study that the WCSPH model is able to encapsulate the double wave group focusing phenomenon in a numerical wave tank; however, there are deficiencies which can be put down to the effects of numerical dissipation.

A grid study was carried out to investigate the convergence of the numerical scheme as well as look at the effect of



numerical dissipation involved. The results of this study are depicted via L2 error plots in Fig. 5. Five different particle resolutions  $\Delta x$  mentioned in Table 1 have been used for this purpose. The L2 error for a particular particle resolution at a certain wave gauge location is computed using the formula

$$L_2(x) = \sqrt{\frac{1}{N} \sum_{i=1}^{N} \left( \eta_{num}(x, t_i) - \eta_{exp}(x, t_i) \right)^2}$$
 (27)

where  $\eta_{num}(x, t_i)$  are the free surface elevation readings obtained from the simulations at a particular location at different time instants,  $\eta_{exp}(x, t_i)$  are the experimental readings and N is the number of observations.

The L2 errors depicted in Fig. 5 have been obtained through interpolation between the different fluid particle resolutions  $\Delta x$  using the in-built MATLAB 'fit' function using a smoothing parameter of 0.9999. The interpolated errors at x = 3m show a decreasing trend, indicating the

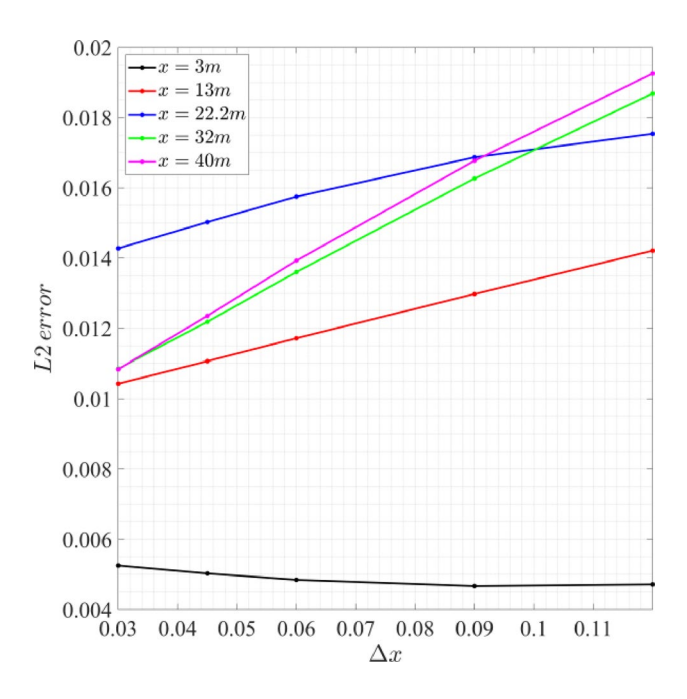


**Fig. 5** Grid study showing the L2 errors interpolated over the range of particle resolutions for the different wave gauge locations used in the numerical simulations of the double focusing wave groups

grid indifference at small distances from the wave maker. At larger distances though, the errors show a gradual increasing trend with decreasing resolution. The L2 error plots reveal that as the distance of wave propagation increases, the errors generally start to increase owing to the numerical dissipative nature of the scheme. The higher error at the focus position of x = 22.2m can also be attributed to this feature. In general, the error plots reveal that our chosen numerical scheme performs reasonably well at a wide range of particle resolutions till wave propagation distances around 10 - 15m from where numerical dissipation starts having an effect on the simulation results.

# 3.2 Numerical experiments for parametric study of perturbed plane waves

The numerical scheme thus validated has been then utilized for carrying out investigations on modulated, unidirectional regular waves in the NWT. The simulation setup is based on the experiments detailed out in Eeltink et al. [16]. For the two-dimensional simulations in the current study, a numerical wave flume of length 33.5m with a water depth of d = 1.2m is used. A piston wavemaker of height of 3.0m is installed at the left of the tank for wave generation and a sloping beach is provided at the end of the tank to facilitate passive wave absorption, similar to the approach used in the work of Altomare et al. [4]. 23 wave gauges are installed along the length of the wave tank as depicted in Fig. 6. The simulation parameters used in these simulations are provided in Table 3.

A total of 22,467 particles constitutes the simulation domain when the fluid particle resolution  $\Delta x$  was  $4 \times 10^{-2}$  m. This is the particle resolution that has been used for all our subsequent results and observations.

The surface elevation readings at the different wave gauge locations for the different numerical experiments have been obtained and analyzed using the different approaches outlined in §2. The observations from these analysis efforts are aimed at examining the effect of the different parameters associated with the generation and propagation of modulated plane waves, with a particular emphasis on the influence of the perturbation sidebands  $(b_F, \alpha)$ , modulational frequency.

 $\Omega_M$  and the effect of water depth d used in our simulations.

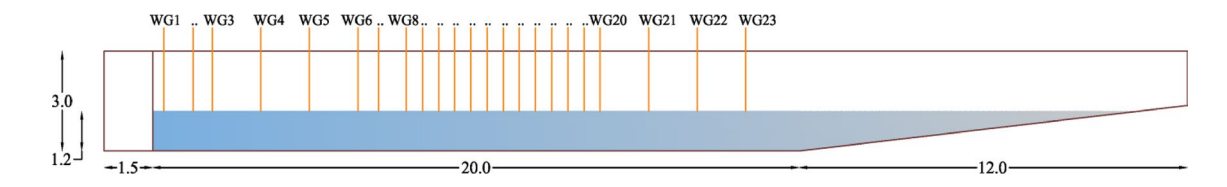


Fig. 6 Numerical setup for parametric study of the plane perturbed waves. All dimensions are provided in meters. 23 wave gauges have been used for these simulations



A total of 40 numerical experiments have been implemented using the different wave parameters outlined in Table 4. The effect of a particular parameter is investigated through its variation over its range while keeping the other parameters constant. The effect of water depth d on the wave propagation has been investigated by carrying out a different series of simulations where a water depth d = 0.8mis used with all other dimensions resembling the numerical setup illustrated in Fig. 6. The same set of parameters given in Table 4 has been implemented in these simulations for comparison purposes. The parameters kept fixed during these different sets of comparisons for the variation of the single parameter in discussion is displayed in boldface in Table 4. The results from the subsequent analyses using simulation observations for the different parameters are presented below.

## 3.2.1 Sideband fraction $(b_F)$

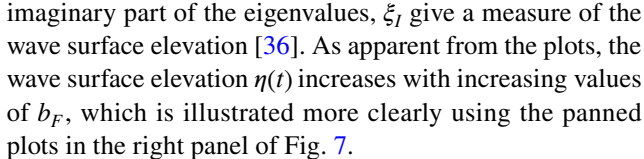
The sideband fraction parameter  $b_F$ , as outlined in Eq. 15 determines the amplitudes of the carrier modes and the frequency sidebands. As can be clearly seen from Eq. 15, larger the value of  $b_F$ , smaller is the amplitude of the carrier mode and larger is the amplitude value of the frequency sidebands for a fixed value of the sideband imbalance parameter  $\alpha$ . For the simulations, the values of  $b_F$  are varied between 0.01 and 0.2 while the other fixed parameters are those that have been depicted in red in Table 4. The time series of the simulation observations are then used for carrying out eigenvalue analysis as discussed in §2. The eigenvalue spectra for four different values of  $b_F$  at x = 4.8m is presented in Fig. 7. The

**Table 3** The simulation parameters in the WCSPH numerical setting used for the parametric studies on the perturbed plane waves. Other simulation parameters are the same as given in Table 1

$\Delta x$	Fluid particle resolution	$\in \{2\times 10^{-2}m, 4\times 10^{-2}m\}$
	Courant number	€ {0.00075, 0.0015}
$\delta$	$\delta$ – SPH coefficient	0

**Table 4** The wave parameters for the different simulations used in the parametric studies of the plane perturbed waves

Perturbation parameters	Notations	Values	Discussion section
Sideband fraction	$b_F$	$\in \{0.01, 0.05, 0.1, 0.15, 0.2\}$	§3.2.1
Sideband imbalance	$\alpha$	$\in \{-0.2, -0.1, 0, 0.08, 0.16\}$	§3.2.2
Relative phase	Φ	$\in \left\{0, \frac{\pi}{2}, \boldsymbol{\pi}, \frac{3\pi}{2}, 2\pi\right\}$	§3.2.3
Carrier frequency	$f_0$	$\in \{0.4Hz, 0.8Hz, \mathbf{1.2Hz}, 1.6Hz, 2.0Hz\}$	§3.2.4
Initial steepness	$\widetilde{a}_0 k_0$	$\in \{0.05, 0.12, 0.18, 0.24, 0.3\}$	§3.2.5
Modulational frequency	$\Omega_M$	$\in [0.001, 2.0, 10.0]$	§3.2.6
Water depth	d	$\in \{0.8, 1.2\}$	§3.2.7



As apparent from Eq. 14, the energy at the wavemaker gets distributed between the carrier modes and the frequency sidebands according to the value of  $b_F$ . Larger the values of  $b_{\rm F}$ , larger are the relative amplitudes of the sidebands in relation to the carrier mode, with the total amplitude remaining the same. When  $\alpha = 0$ , as is the case in these simulations for the variation of  $b_F$ , the sideband amplitudes are only dependent on  $b_F$ , which ultimately decides the wave propagation behavior over the NWT. The observations in Fig. 7 suggest that larger the amplitudes of the sidebands in relation to the carrier mode at the wavemaker, larger is the overall wave amplitude at increasing distances from the wavemaker. Thus, it can be ascertained that higher energy in the frequency sidebands at the wavemaker result in higher wave amplitudes than a single carrier wave. The energy distribution in the different frequency modes can also be visualized through frequency spectrum plots as illustrated in Fig. 8a. The mean wave amplitudes, obtained as discussed in §3.2, are plotted at the different wave gauge locations for all the values of  $b_F$ and depicted in Fig. 8b. From Fig. 8a, it can be observed that when  $b_F = 0.01$ , the carrier mode has the maximum amount of energy being transmitted at the wavemaker which gets propagated through the NWT. As the value of  $b_F$  increases, the relative influence of the sidebands grows compared to the carrier mode, particularly that for the lower frequency sideband. The lower sideband can be observed to propagate throughout the length of the NWT, which is not observed for the carrier mode in any of the above simulations. The increased energy in the sidebands lead to larger wave amplitudes as can be observed clearly from the plots in Fig. 8b. Till around x = 9m in the NWT, the time averaged wave amplitudes are seen to increase with increasing values of  $b_F$ till  $b_F = 0.15$ . Subsequent increase in the values of  $b_F$  does not lead to significant growth in amplitudes, which is also noted from the frequency spectra plots for  $b_F = 0.15$  and



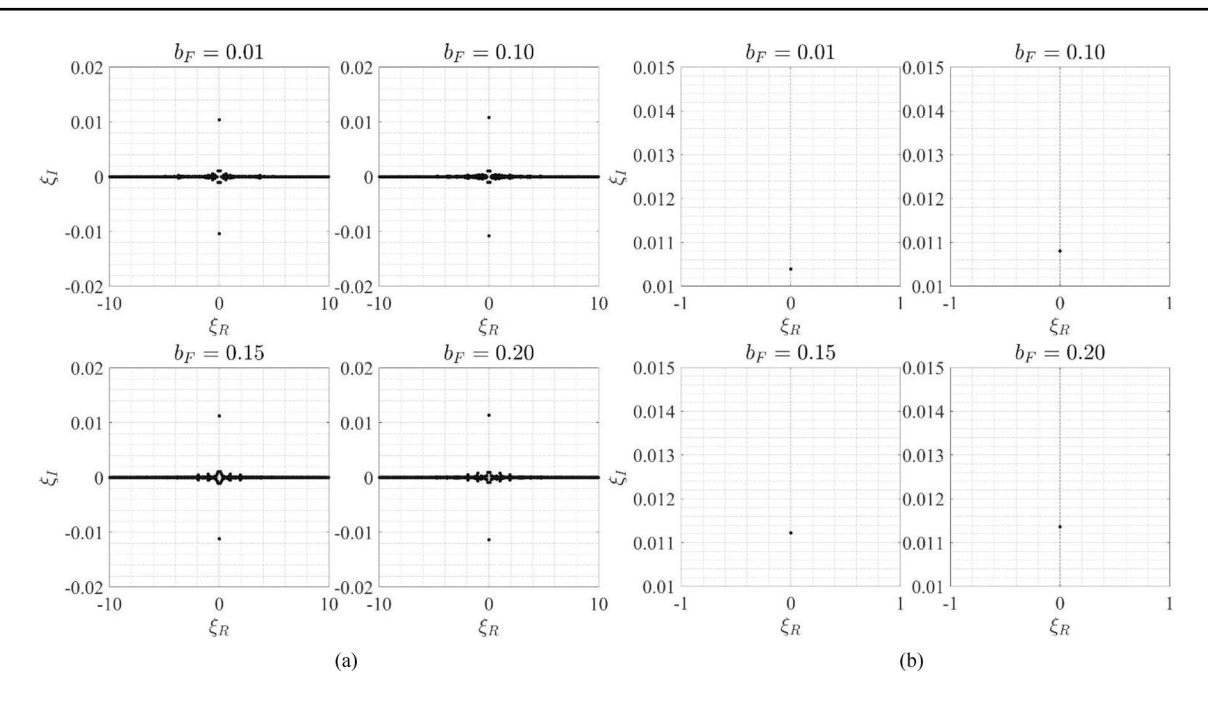
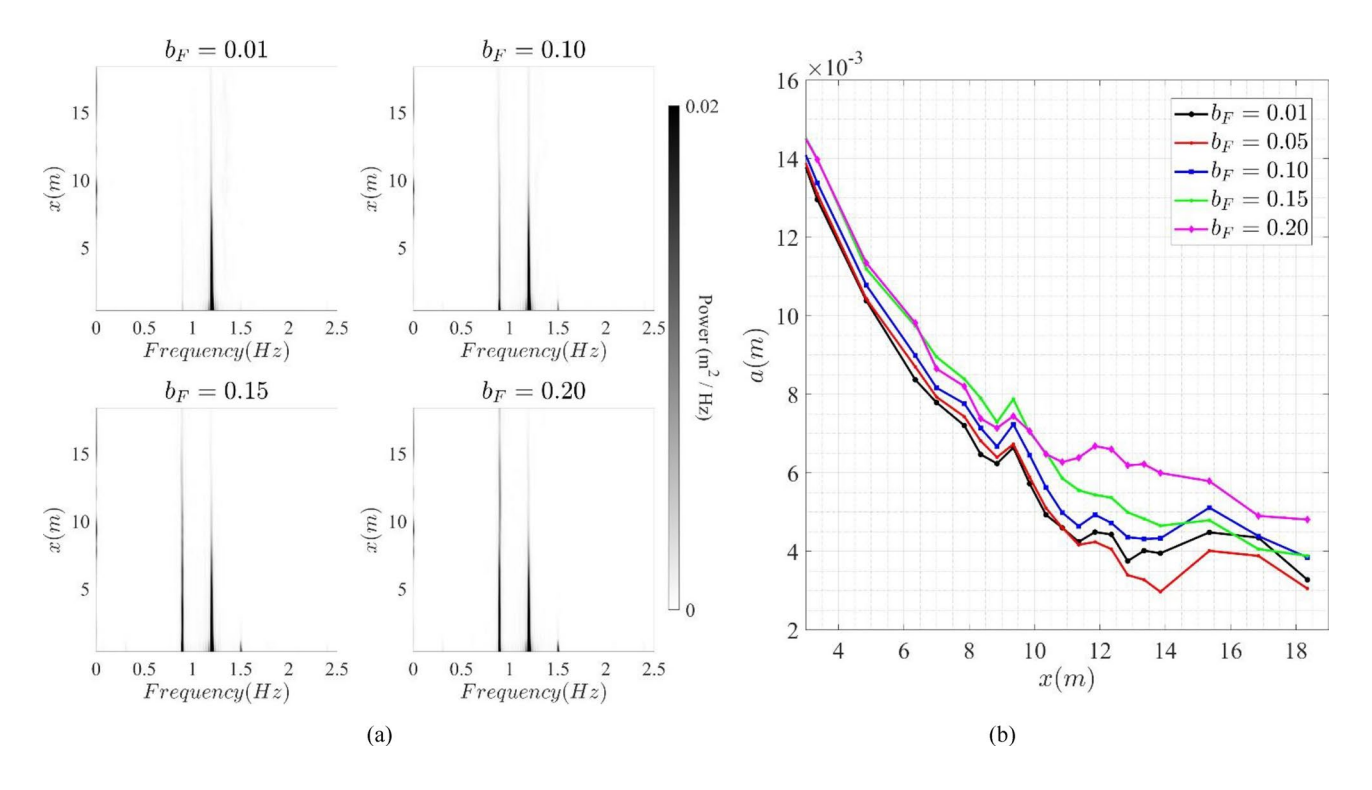


Fig. 7 The eigenvalue spectra for 4 different values of  $b_F$  used in the numerical simulations. The left panel depicts the spectra within a range of  $\xi_R$  from -10 to 10. The right panel shows a zoomed version of the plots in the left panel for  $\xi_I$  ranging from 0.01 to 0.015 for better visualization



**Fig. 8** a Frequency spectrum values for 4 different values of  $b_F$ . The plots give the energy distribution over the length of the wave tank for the different frequency values. **b** The time averaged wave amplitudes

for the different values of  $b_{\it F}$  at the different gauge locations along the wave tank



 $b_F = 0.20$  in Fig. 8a. It can thus be ascertained that increased energy in perturbation sidebands leads to elevated wave amplitudes for a modulated plane propagating wave, with the lower sideband in particular, having a prominent effect on the wave propagation nature. The marked disparity between the sidebands observed during the wave propagation in the above simulations were investigated through the variations of the sideband imbalance  $\alpha$ , which is discussed next.

#### 3.2.2 Sideband imbalance (a)

The sideband imbalance, as expressed in Eq. 15 determines the relative influence of the two frequency sidebands on the resultant wave amplitude. As can be seen from Eq. 15, for a fixed carrier mode amplitude, larger the sideband imbalance  $\alpha$ , larger is the amplitude of the higher frequency sideband and conversely, the energy transferred to the lower frequency sideband at the wavemaker decreases. To observe the relative effect of the two perturbation sidebands, simulations are carried out by varying the values of  $\alpha$  between -0.2 and 0.16 while keeping the other parameters fixed as depicted in Table 4. Similar to the study of  $b_F$ , eigenvalue analysis was also carried out at x = 4.8m for the different values of  $\alpha$ . The eigenvalue spectra for these simulations are depicted in Fig. 9. As the imaginary part of the eigenvalues,  $\xi_I$  give a measure of the wave surface elevations obtained from the observation time series, it can be ascertained from the plots in Fig. 9 that increase in sideband imbalance results in a decrease of wave amplitudes at non-zero distances from the wavemaker. For  $\alpha = 0$ , the two perturbation sidebands are

equal in magnitude at the wavemaker. As  $\alpha$  becomes positive, more energy is provided to the higher frequency sideband at the wavemaker. As depicted in the plots for  $\alpha = 0.08$  in Fig. 9, there is a marked decrease in  $\xi_I$  and consequently, the wave surface elevation at x = 4.8m compared to  $\alpha = 0$ . On the other hand, when  $\alpha$  becomes negative, a larger portion of the energy at the wavemaker is given to the lower frequency perturbation relative to the higher sideband. From the plots for  $\alpha = -0.1$  and  $\alpha = -0.2$  in Fig. 9, it can be observed that the  $\xi_I$ values are higher than that for  $\alpha = 0.08$ , signifying that larger waves are observed as  $\alpha$  tends to more negative values. These observations suggest that there is significantly lower energy decay when fed to the lower frequency sideband compared to the higher frequency perturbation in the propagation of such plane perturbed waves in our NWT. Consequently, the observed wave surface elevations are higher when the values of  $\alpha$  become more negative. Furthermore, as can be observed from the plots in Fig. 9b, there is a marked increase in wave surface elevation from  $\alpha = -0.1$  to  $\alpha = -0.2$  compared to the elevation when the values are decreased from  $\alpha = 0$  to  $\alpha = -0.1$ . This signifies that at lower absolute values of  $\alpha$ , the wave propagation is dominated by the effect of the sideband fraction  $b_F$ . However, as the value of  $\alpha$  gets more negative, the asymmetry in the sidebands has a more pronounced effect on the wave propagation scenario compared to the sideband fraction  $b_F$ .

To further look at the asymmetric nature of the perturbation sidebands during the plane wave propagation, the energy distribution in the different frequency modes along the NWT is illustrated with the help of frequency

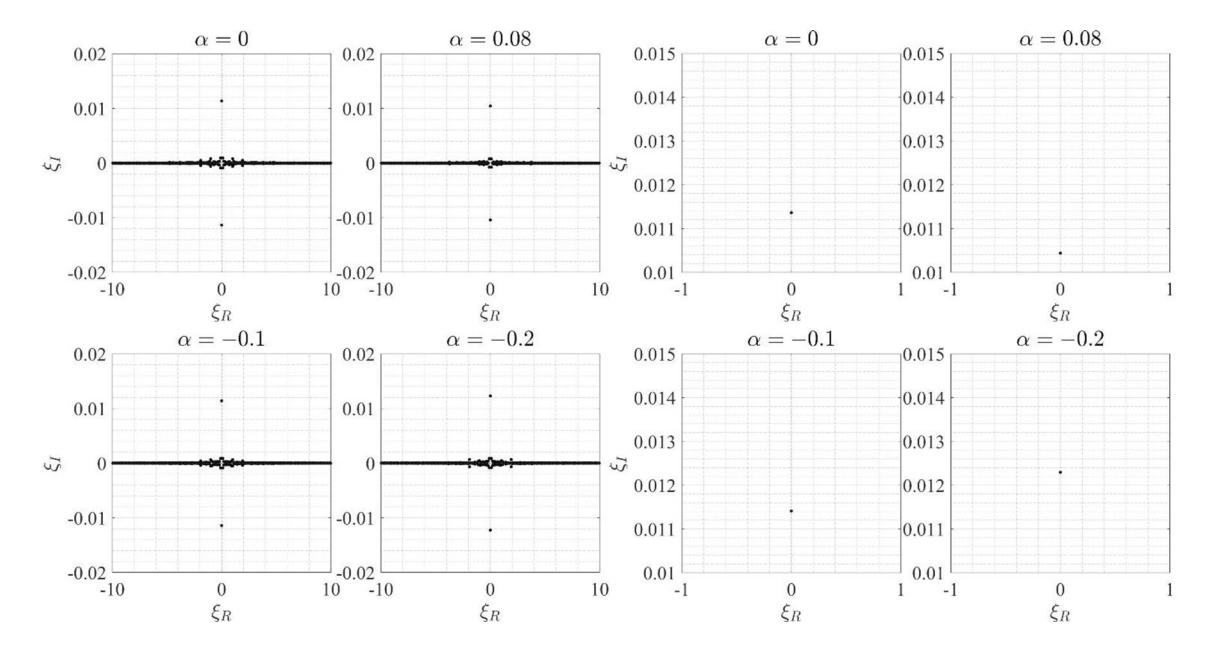


Fig. 9 The eigenvalue spectra for 4 different values of  $\alpha$  used in the numerical simulations. The left panel depicts the spectra within a range of  $\xi_R$  from -10 to 10. The right panel shows a zoomed version of the plots in the left panel for  $\xi_I$  ranging from 0.01 to 0.015 for better visualization



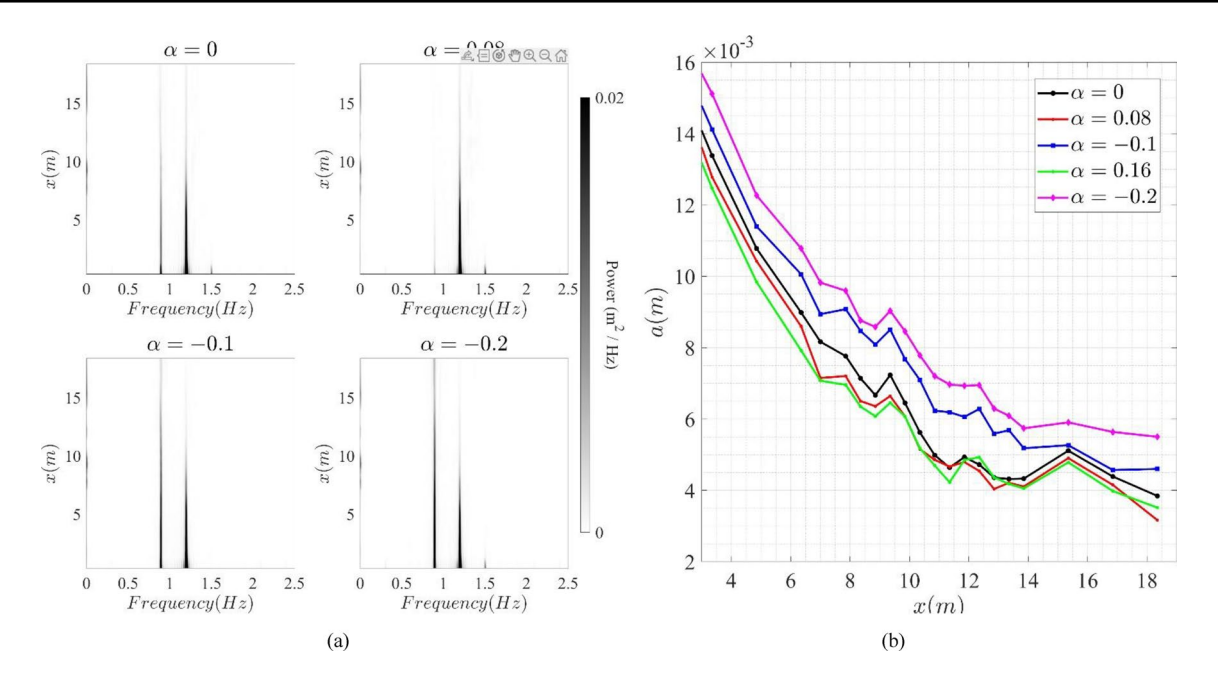


Fig. 10 a Frequency spectrum values for 4 different values of  $\alpha$ . The plots give the energy distribution over the length of the wave tank for the different frequency values. **b** The time averaged wave amplitudes for the different values of  $\alpha$  at the different gauge locations along the wave tank

spectrum plots in Fig. 10a. The mean amplitude variation along the wave tank is also depicted in Fig. 10b. The frequency spectrum plots in Fig. 10a consolidate the observations in Fig. 9. It can be observed that as the values of  $\alpha$ get more negative, a larger amount of energy is transferred to the lower frequency sideband that propagates over the length of the NWT. The energy decay is much more prominent for the higher frequency sideband that results in lower energy values further down the NWT when  $\alpha$ is positive. The mean surface amplitudes at the different wave gauge locations are displayed in Fig. 10b. The plots reiterate our observations that wave amplitudes decrease with increasing  $\alpha$ , showing the influence of the lower frequency sideband in the wave evolution for such perturbed plane wave scenarios. The energy patterns in the different frequencies during the wave evolution is further elucidated through the wavelet energy spectrum method, which was discussed during our validation efforts. The WES plots in Fig. 11 depict the energy spectra at 4 different gauge locations for  $\alpha = 0.16$  and  $\alpha = -0.2$ . The comparison of the plots at x = 0.35m reveal that the energy distribution close to the wavemaker are similar for both the values of  $\alpha$ , signifying that the energy input from the wavemaker do not determine the asymmetric behavior of the sidebands. However, with wave propagation along the wave tank, disparities in energy distribution show up. The dominance of the higher sideband is clearly visible for  $\alpha = 0.16$  at x = 4.85m. However, this begins to break up farther away from the wavemaker, and the energy and consequently, the wave amplitude starts diminishing. On the contrary, for

 $\alpha = -0.2$ , the energy of the lower sideband becomes significant at x = 4.85m. With increasing distance, the lower sideband continues to remain dominant, as a consequence of which the wave amplitudes are higher over the wave tank than for  $\alpha = 0.16$ .

#### 3.2.3 Relative phase (Ф)

This parameter, given in Eq. 14 determines the relative phase between the carrier mode and the frequency sidebands. The fixed wave parameters used for these simulations are given in Table 4. The values of  $\Phi$  are varied between 0 and  $2\pi$ . As done before, frequency spectrum plots and mean amplitude plots are created for different values of  $\Phi$ . These are illustrated in Figure.

12. The plots in Fig. 12a reveal that there are negligible differences between the different values of  $\Phi$  when energy distribution is considered for the different frequency bands. In all the cases, there is visible energy localization in the lower frequency sideband. However, with the increase of  $\Phi$ , the rate of energy decay over the NWT in the lower sideband shows a decreasing trend. The mean amplitude plots given in Fig. 12b help consolidate the observations of the frequency spectrum plots depicted in Fig. 12a, showing that the results obtained by using the various values of  $\Phi$  at different gauge locations are similar. This shows that the relative phase between the carrier and sidebands does not significantly influence wave propagation in our simulation scenarios. However, the influence of the lower frequency



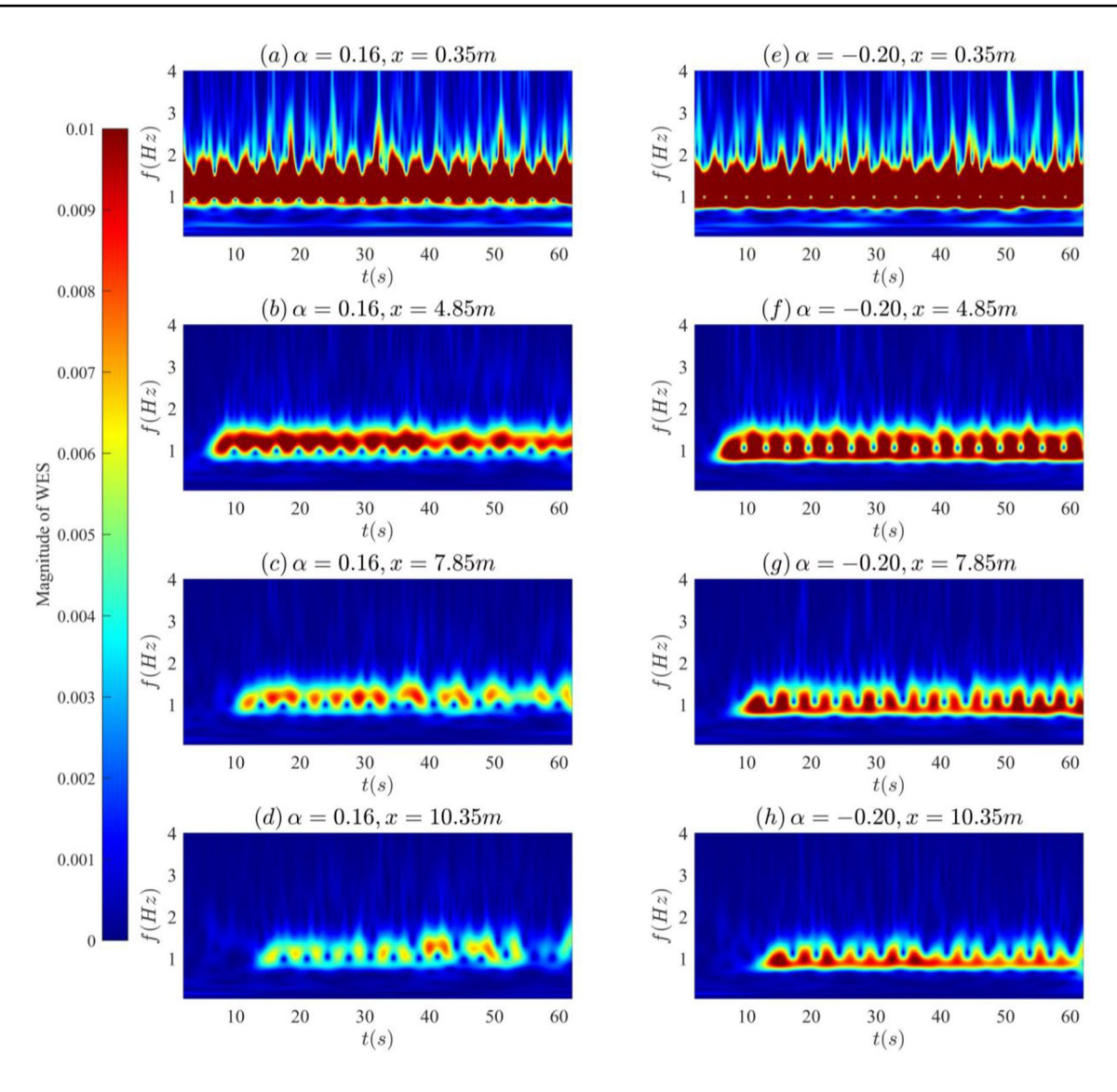


Fig. 11 WES plots for two different values of  $\alpha$  at 4 different locations along the numerical wave tank. The left panel (**a-d**) displays the results for  $\alpha = 0.16$  and the right panel (**e-h**) depicts the results for  $\alpha = -0.2$ 

perturbation is still apparent from these observations, pointing to the asymmetric nature of the perturbation sidebands.

#### 3.2.4 Carrier mode frequency ( $f_0$ )

The influence of the carrier mode frequency depicted in Eq. 14 on the wave evolution has been also investigated through a different set of simulations. For all these simulations, the resultant wavenumbers are found out using the frequency dispersion relation as follows.

$$\omega^2 = gk \ tanh(kh) \tag{28}$$

where,  $\omega$  is the carrier wave frequency, g is the acceleration due to gravity, k is the associated wavenumber and h

is the water depth in the NWT. The fixed wave parameters used in these simulations for studying the variation of  $f_0$  are given in Table 4. The parameter  $f_0$  used for the comparisons was varied between 0.4Hz and 2.0Hz. The time series of the amplitudes at the different gauge locations are illustrated for different values of  $f_0$  through Fig. 13a.

The spatial evolution plots in Fig. 13a show that the wave amplitudes across the wave tank increase with decrease in the carrier mode frequency. However, the high energy involved in the lower frequency cases can be attributed to the carrier mode only as low frequency results in high initial amplitude according to the dispersion relation provided the initial wave steepness is kept constant. The influence of the different modes in the energy distribution along the wave tank is elucidated through WES



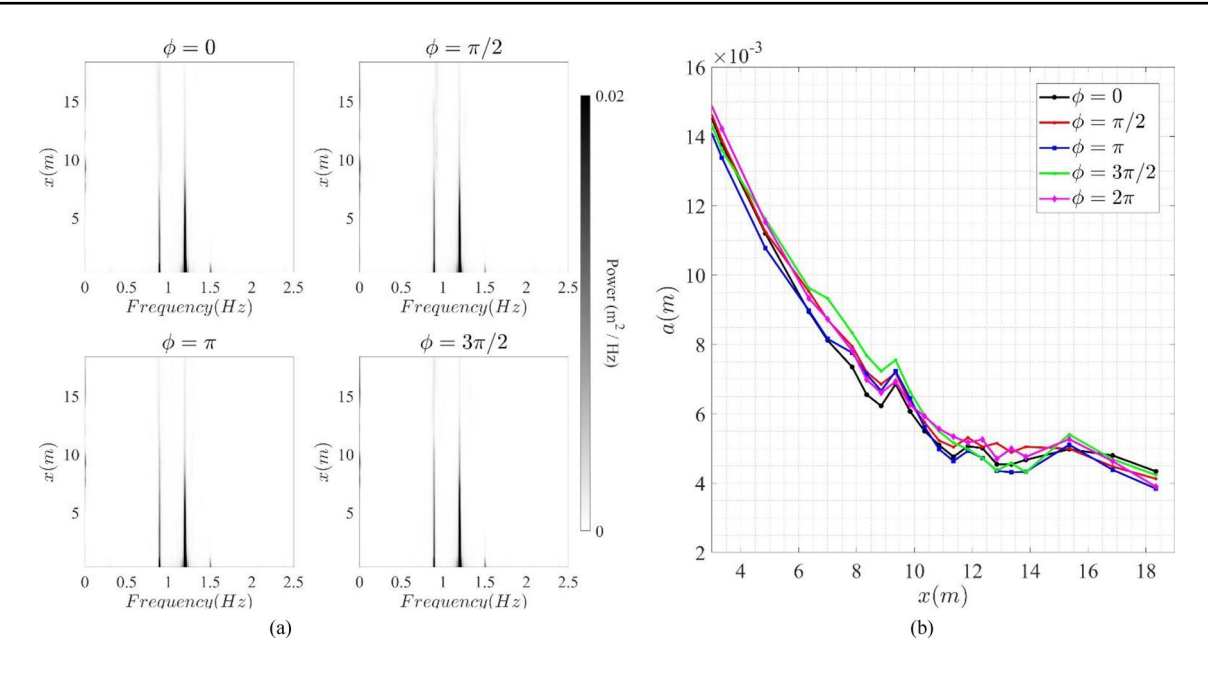
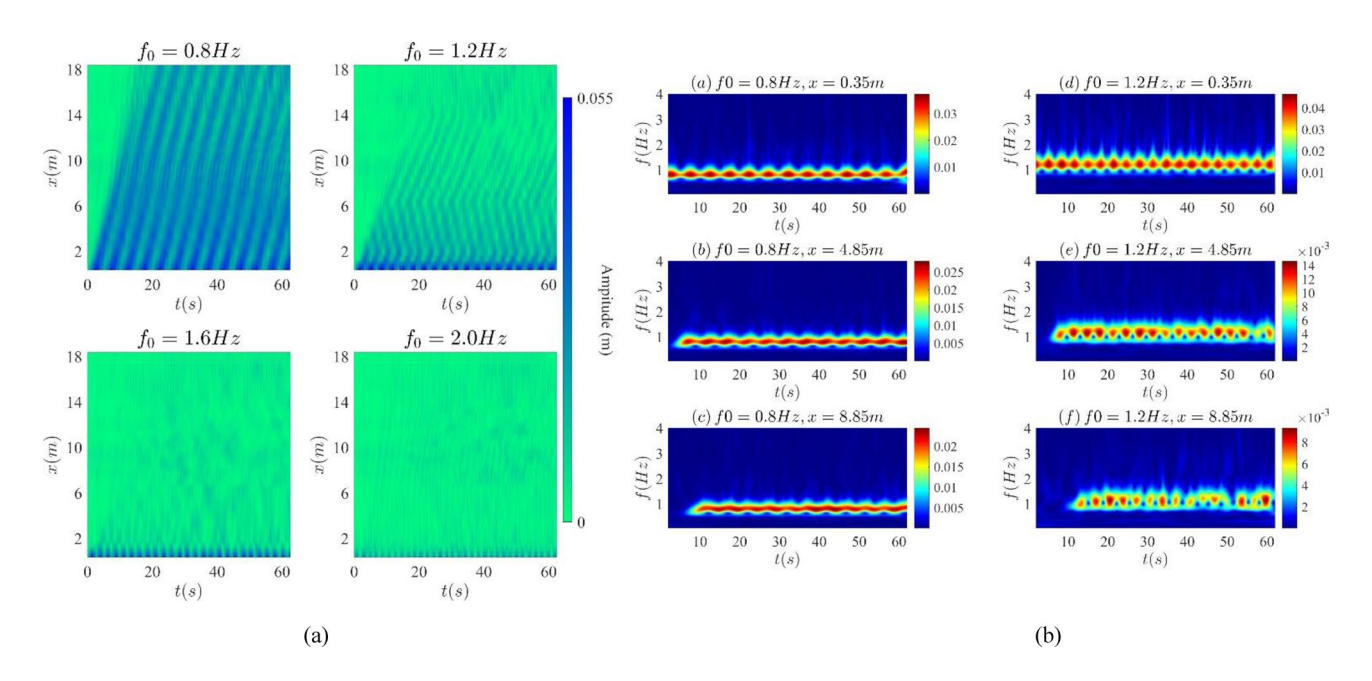


Fig. 12 a Frequency spectrum values for 4 different values of  $\Phi$ . The plots give the energy distribution over the length of the wave tank for the different frequency values, **b** The time averaged wave amplitudes for the different values of  $\Phi$  at the different gauge locations along the wave tank



**Fig. 13 a** Spatial and temporal evolution of the wave amplitudes across the numerical wave tank for 4 different values of  $f_0$ . **b** WES plots for two different values of  $f_0$  at 3 different locations along the

numerical wave tank. The left panel (**a-c**) displays the results for  $f_0$  = 0.8 Hz and the right panel (**d-f**) depicts the results for  $f_0$  = 1.2Hz

plots for  $f_0 = 0.8Hz$  and  $f_0 = 1.2Hz$  in Fig. 13b. As can be seen clearly from the plots, for  $f_0 = 0.8Hz$ , at all the different gauge locations, the energy is primarily concentrated around the main frequency of 0.8Hz. However, for  $f_0 = 1.2Hz$ , transfer of energy can be observed from

the carrier mode to the sidebands as the distance from the wavemaker increases. Thus, it can be ascertained that for lower carrier mode frequencies, sideband perturbation does not significantly influence the evolution of a unidirectional plane wave. On the other hand, sideband



modulation, especially the lower energy sideband has a significant effect on the propagation of plane unidirectional waves with higher carrier frequencies.

### 3.2.5 Initial steepness $(\tilde{a}_0 k_0)$

The initial steepness in Eq. 14 determines the initial wave amplitude if the wave carrier frequency is constant. Simulations are implemented to study the influence of this parameter on the resultant amplitudes of plane perturbed waves. The parameter  $\widetilde{a}_0k_0$  was varied between 0.12 and 0.30 while the other fixed parameters are given in Table 4. Similar to our previous efforts, the obtained surface elevation readings at the different gauge locations were used for calculating the wave amplitudes. The obtained wave amplitudes at the different wave gauge locations are provided in Fig. 14a. The energy distribution among the different frequency modes over the NWT are depicted in Fig. 14b.

As apparent from the plots in Fig. 14a, larger the initial steepness, larger are the wave amplitudes over the NWT in general. Additionally, from the frequency spectrum plots in Fig. 14b, it can be observed that the perturbation sidebands move apart as the initial wave steepness increases. For lower values of  $\tilde{a}_0k_0$ , a larger amount of energy localization can be seen in the higher frequency sideband. As initial steepness increases, the energy localization in the lower frequency perturbation increases, which results in larger wave amplitudes over the NWT. The influence and the asymmetric nature of the

modulation sidebands is thus, further illustrated through these observations.

#### 3.2.6 Modulational frequency ( $\Omega_M$ )

The modulational frequency  $(\Omega_M)$  in Eq. 14 determines the frequency of the perturbations being added to the unidirectionally propagating regular wave in the NWT. Larger the value of  $\Omega_M$ , more disparate are the sidebands from the carrier frequency. Similar to our previously discussed studies, a carrier frequency of 1.2Hz was used for the generation of the plane waves. Perturbations with values ranging from 0.001 to 10.0 have been used for this study. The other associated fixed wave parameters are given in Table 4. The spatial and temporal evolution of the wave amplitudes for the different values of  $\Omega_M$  is illustrated in Fig. 15. The process of modulation can be observed through the onset of the blue patterns in the different plots. For smaller values of  $\Omega_M$ , the perturbations die down at very small distances from the wavemaker at x = 0 and cannot result in elevated wave amplitudes, as can be seen clearly from the plots of  $\Omega_M = 0.001$ ,  $\Omega_M = 0.04$  and  $\Omega_M = 0.075$ . For larger values, the perturbations  $\Omega_M = 5.0$ and  $\Omega_M = 10.0$  give very similar results as apparent from their respective plots.

To gain further understanding on the phenomenon of this modulation, the frequency spectrum plots illustrated in Fig. 16 are used for looking at the energy distribution within the different frequency modes during these simulations. Since the frequency spectrum plots in Fig. 16 are drawn to the same scale, the energy distribution for  $\Omega_M = 0.001$ 

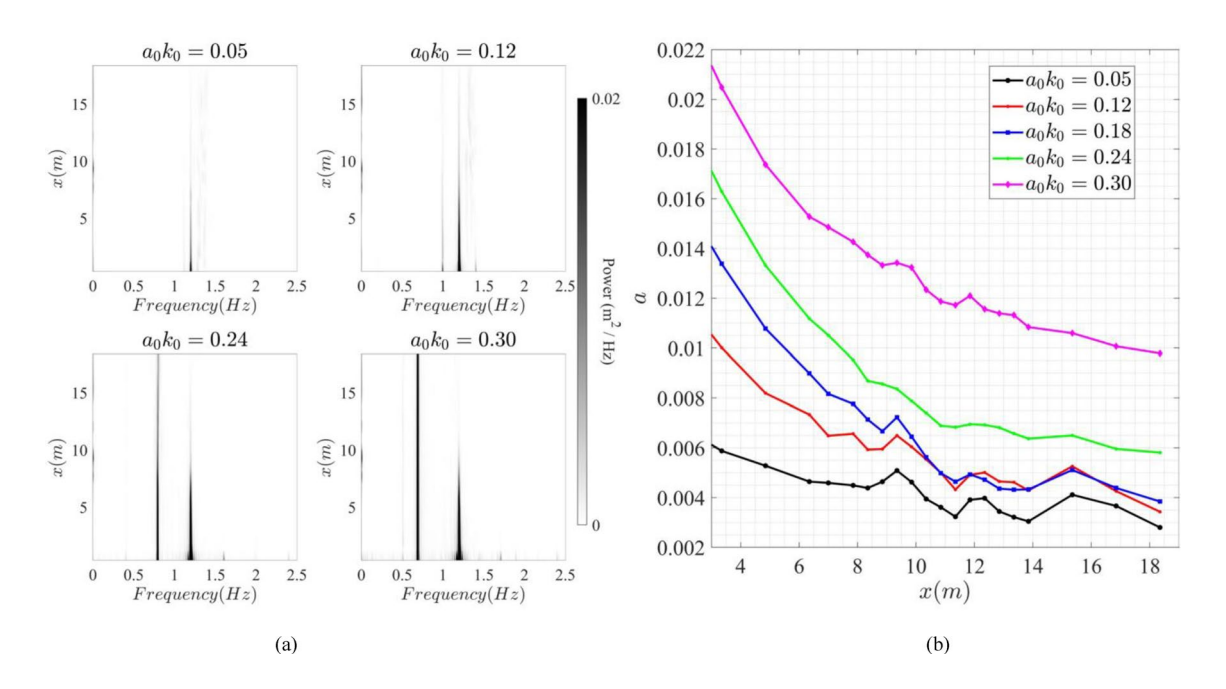


Fig. 14 a Frequency spectrum values for 4 different values of  $\widetilde{a}_0 k_0$ . b The time averaged wave amplitudes for the different values of  $\widetilde{a}_0 k_0$  at the different gauge locations along the wave tank



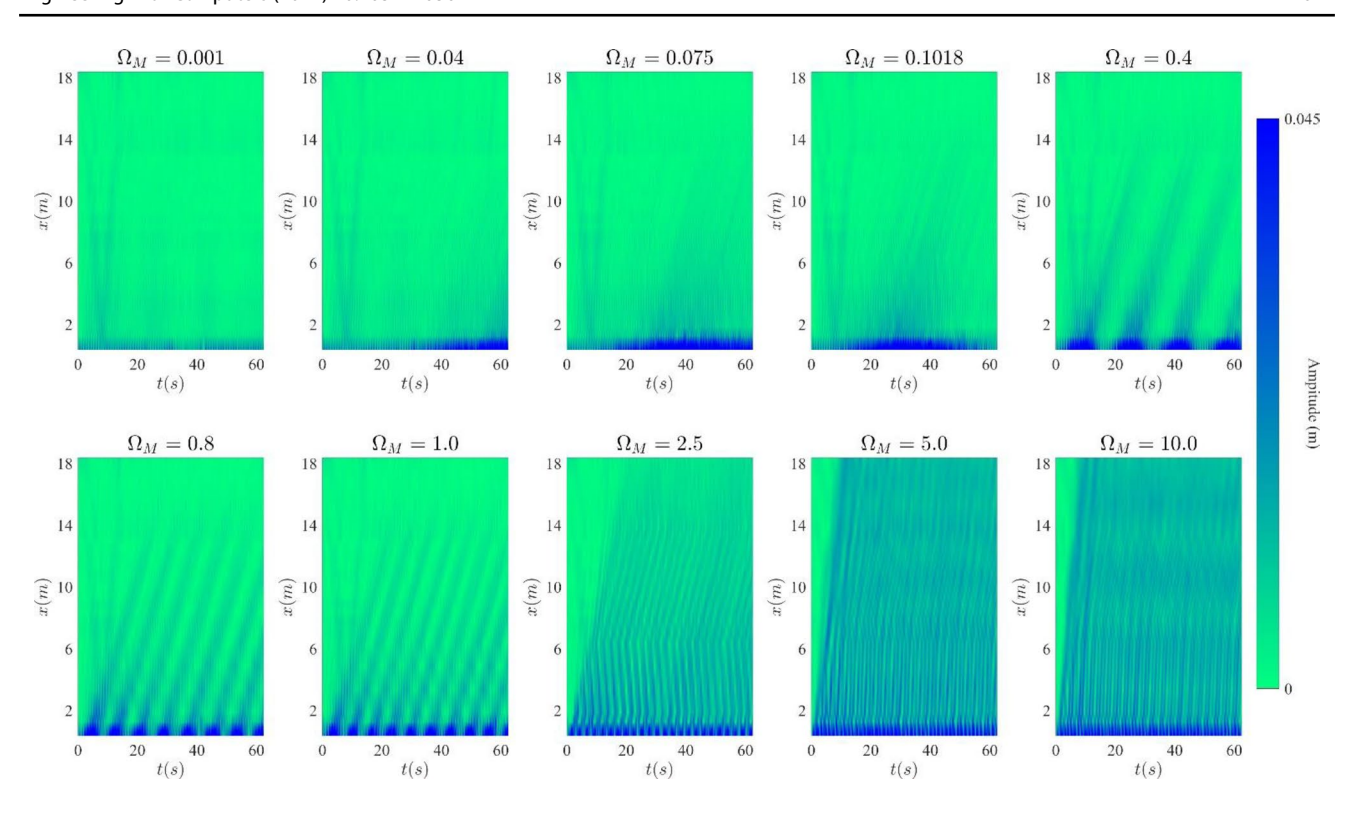


Fig. 15 Spatial and temporal evolution of the wave amplitudes across the numerical wave tank for 10 different values of  $\Omega_M$ 

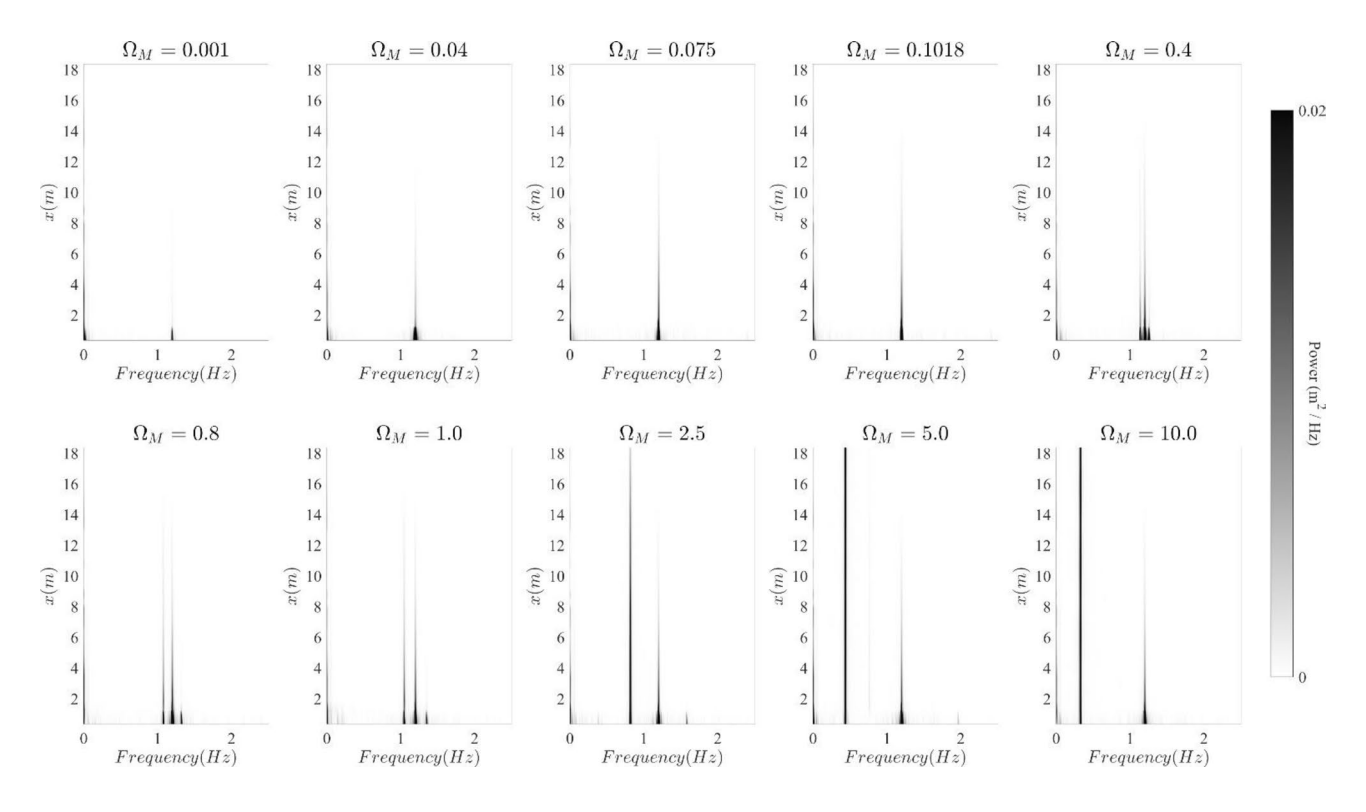


Fig. 16 Frequency spectrum plots of the perturbed plane waves for the different values of  $\Omega_{M}$ 



only shows a faint line for the energy in the carrier mode. As  $\Omega_M$  increases, the energy in the carrier band is seen to increase, but the sidebands are very close to the main frequency mode to be recognized differently. The growth of the sidebands can be seen prominently for  $\Omega_M=0.4$  where the lower sideband displays more growth than the higher sideband. As  $\Omega_M$  increases, the sidebands start to get apart from one another and more energy localization is observed in the lower sideband. Particularly, for  $\Omega_M=5.0$  and  $\Omega_M=10.0$ , it can be clearly observed that there is a lot of energy localization in the lower frequency sideband, leading to growth of wave amplitudes. The energy growth patterns resemble that of the spatial evolution plots in Fig. 15, which shows that there is very little wave growth above a certain value of the modulational frequency  $\Omega_M$ .

The mean wave amplitudes at the different locations along the wave tank are depicted in Fig. 17a to consolidate the observations in Fig. 15. In addition, the WES plots of  $\Omega_M=1.0$  and  $\Omega_M=2.5$  are compared at 3 different locations to better visualize the results illustrated through Fig. 18.

The plots of the mean amplitudes at the different gauge locations in Fig. 17a suggest that the mean amplitudes grow with increasing  $\Omega_M$  till  $\Omega_M=5.0$ . However, further increase of  $\Omega_M$  to 10.0 does not result in increased wave amplitudes and the maximum of wave amplitude oscillates between  $\Omega_M=5.0$  and  $\Omega_M=10.0$  at the different wave gauge locations.

These results point to the fact that wave amplitudes do not get modified significantly by modulations when the modulational frequency parameter goes beyond a certain threshold value. In this case, the ratio of the modulational frequency  $\Omega_M$  and the carrier frequency parameter  $f_0$  is around 4.167. The energy spectrum plots in Fig. 17b reveal the evolution of energy distribution between the carrier and the sidebands for two values of  $\Omega_M$ . The plots for  $\Omega_M = 1.0$  at the different locations suggest that there is very little energy transfer from the carrier mode to the sidebands. On the contrary, for  $\Omega_M = 2.5$ , the transfer of energy from the carrier frequency of  $1.2H_Z$  to the lower sideband  $0.95H_Z$  can be observed to start occurring at x = 4.85m and starts getting more prominent with increasing distance from the wavemaker, and this finally results in the increased wave amplitudes compared to the case of  $\Omega_M = 1.0$ .

#### **3.2.7** *Effect of water depth* (*d*)

The impact of water depth d on the effect of the different parameters during the propagation of plane, perturbed waves has been also investigated through a different set of simulations. As mentioned in §2, the same set of numerical simulations have been also implemented in the NWT for a water depth of d = 0.8m. The results for the different sets of parameters are discussed below.

The plots in Fig. 18a compare the eigenvalue spectra for the two water depths using the surface elevation time series  $\eta(t)$  for  $b_F = 0.1$  and  $b_F = 0.2$  at a location of x = 4.8m down the numerical wave tank. It can be observed that for both the values of the parameter, the

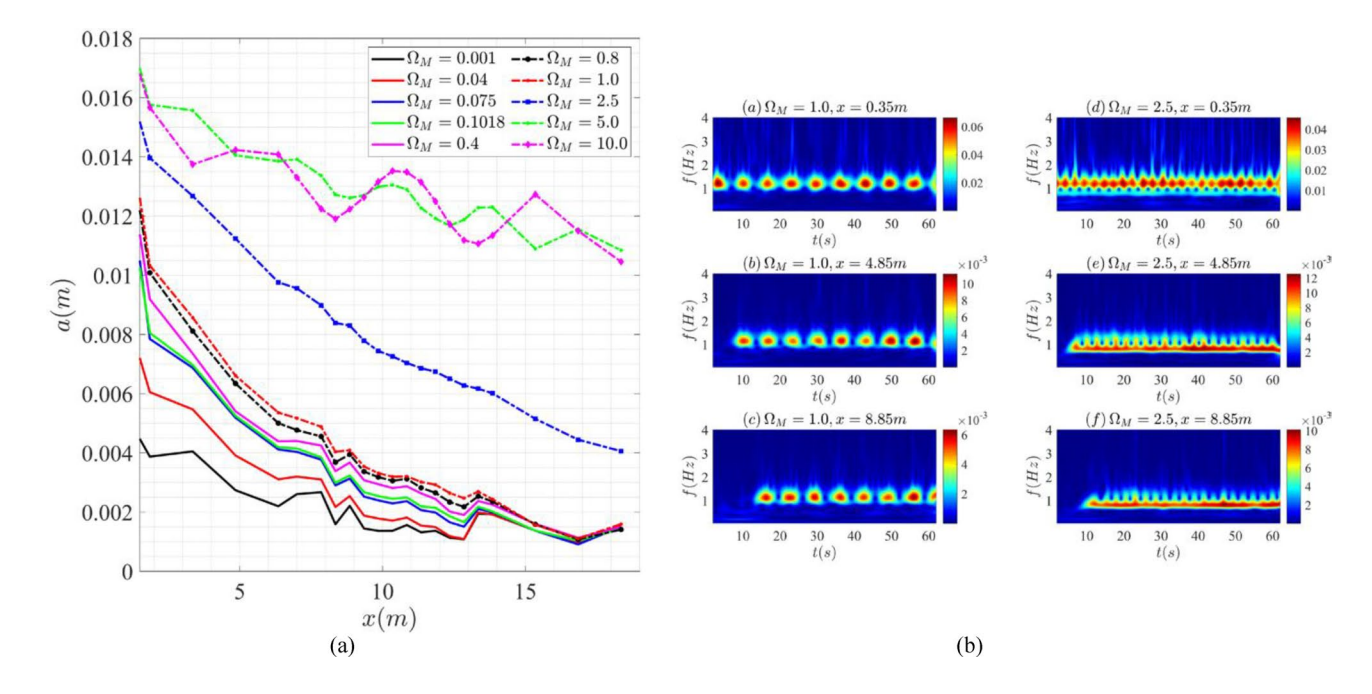


**Fig. 17** a The time averaged wave amplitudes for the different values of  $\Omega_M$  at the different gauge locations along the wave tank. **b** WES plots for two different values of  $\Omega_M$  at 3 different locations along the

numerical wave tank. The left panel (**a-c**) displays the results for  $\Omega_M=1.0$  and the right panel (**d-f**) depicts the results for  $\Omega_M=2.5$  Frequency spectrum values for 4 different values of  $\Omega_M$ 



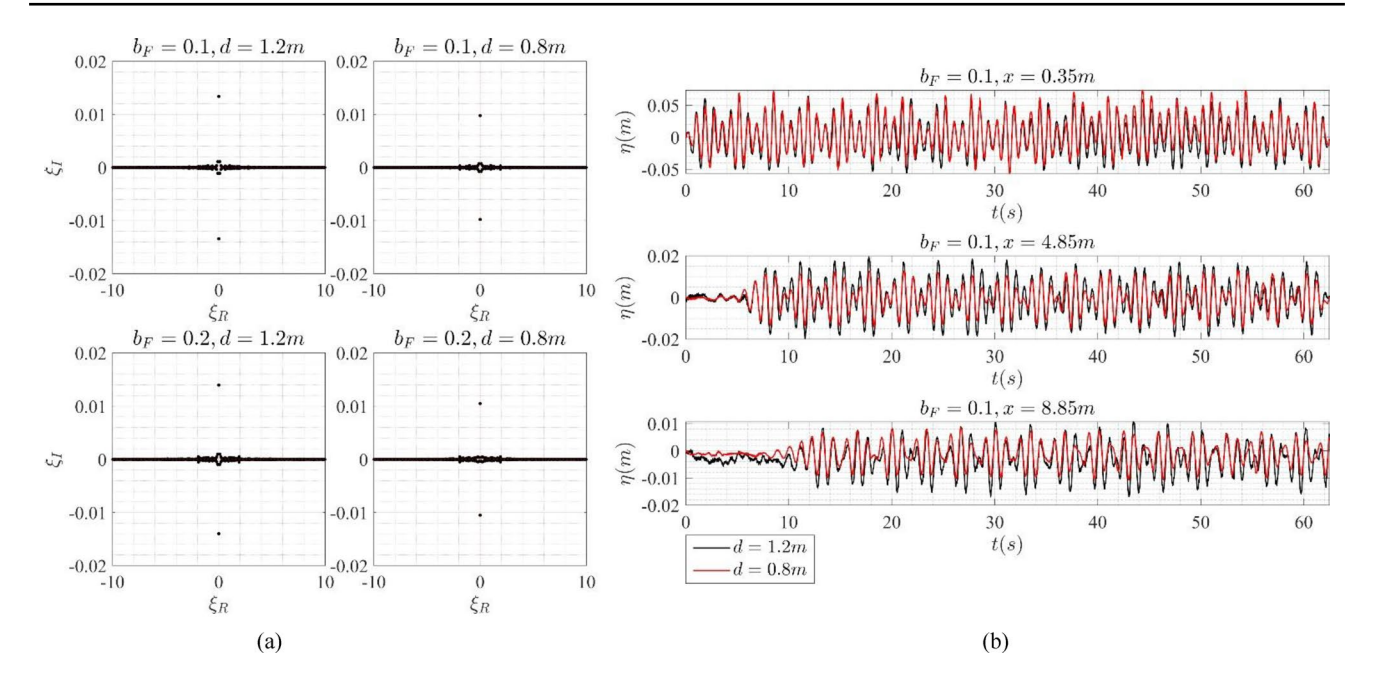


Fig. 18 a Eigenvalue spectrum for two values of  $b_F$  for d=1.2 m and d=0.8 m (b) The surface elevation comparisons between d=1.2 m and d=0.8 m for  $b_F=0.1$  at 3 different locations

wave elevation is much higher for d=1.2m compared to d=0.8m. To visualize the wave evolution differently, the surface elevation plots for  $b_F=0.1$  at 3 different locations is presented in Fig. 18b for the two water depths. It can be seen that at x=0.35m, the elevation pattern for the two water depths resembles each other closely. However, as the distance increases, the crests and troughs for d=0.8m begin to get shorter in comparison to d=1.2m x=8.85m. This is more pronounced for the plots at , where the troughs in between peaks are observed to die

down. These observations suggest that perturbations to a regular, unidirectional wave have a reduced effect for decreasing water depths.

Similar to Fig. 18b, comparisons between the two water depths for  $\Omega_M = 1.6$  at different locations are illustrated in Fig. 19a. The observations resemble the results from Fig. 18b. As the distance from the wavemaker increases, the crests and troughs become shorter for d = 0.8m when compared to d = 1.2m, with more disparities being observed between the two sets. This again points to the

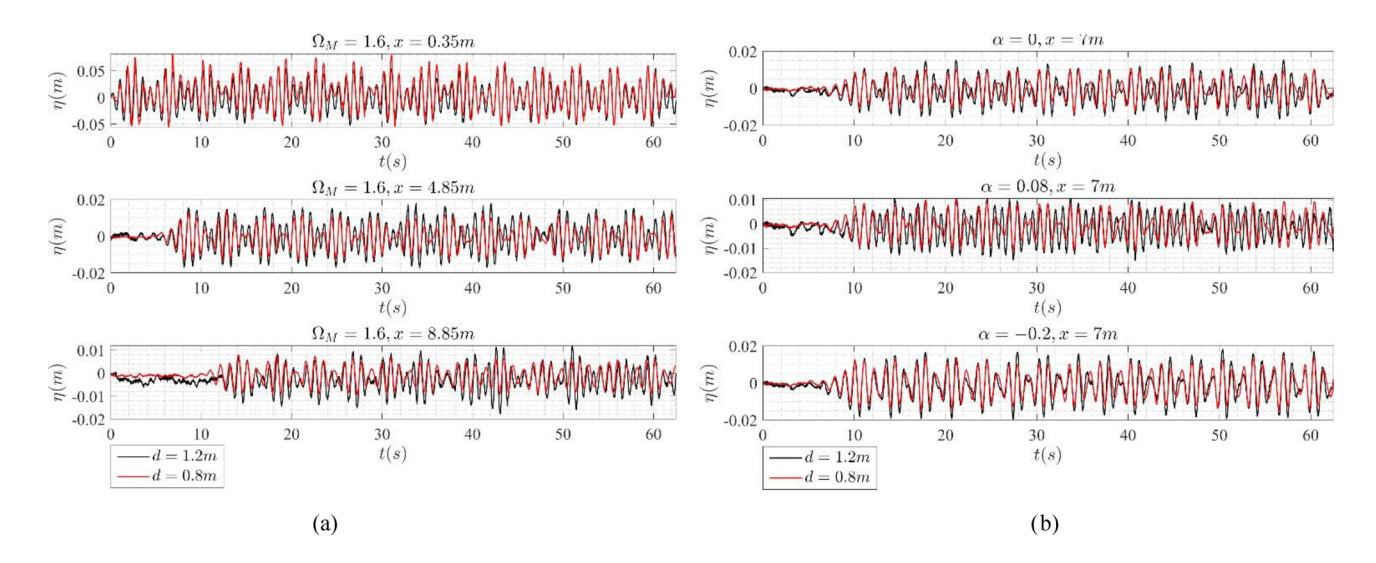


Fig. 19 a Surface elevation comparisons between d=1.2 m and d=0.8 m for  $\Omega_M=1.6$  at 3 different locations (b) Surface elevation comparisons between d=1.2 m and d=0.8m at x=7m for  $\alpha=0$ ,  $\alpha=0.08$  and  $\alpha=-0.2$ 



reduced modulational effects on unidirectional regular waves with decreasing water depth d. The variation of the sideband imbalance ( $\alpha$ ) parameter in Fig. 19b for a fixed wave gauge location reveals the impact of  $\alpha$  during plane, perturbed waves propagation. As observed in Fig. 19a, the plots show that the wave elevation is smaller for d=0.8m for all the values. However, it can also be seen that positive values of  $\alpha$  lead to greater variation in the elevations for the two depths compared to a negative value of  $\alpha$ . For  $\alpha=-0.2$ , the gulf between the two sets of values is much lower than that for  $\alpha=0.08$  and  $\alpha=0$ . These observations demonstrate that the effect of perturbation, though diminished, still applies for lower water depths in these simulations.

To gain further insight into the perturbation process for varying depths, the observations for the simulations implementing different initial steepness  $\tilde{a}_0 k_0$  and carrier frequencies  $f_0$  are illustrated in Figs. 20a, b respectively. The plots in Fig. 20a show that as the initial wave steepness  $\tilde{a}_0 k_0$ increases, the peaks, and troughs for the two water depths dstart approaching each other. On the contrary, in Fig. 20b, as the carrier frequency  $f_0$  increases, the obtained surface elevation readings for the d = 0.8m diminish at a much faster rate when compared to d = 1.2m. These observations can be attributed to the following. Firstly, as the initial wave steepness  $\tilde{a}_0 k_0$  increases, the initial wave amplitude also increases which results in shallower sea scenarios. For the two different water depths d, thus, higher initial steepness  $\tilde{a}_0 k_0$  results in similar wave propagation scenarios, thus rendering similar results. On the other hand, higher carrier wave frequency  $f_0$ , according to the frequency dispersion relationship, results in lower initial wavelengths. This results in deeper sea environments, and the surface elevation readings for lower depths are much lower than that for higher water depths. These observations help us inferring that modulations can significantly affect the evolution of regular unidirectional waves in deep sea waters, while moving to shallower seas reduces the effect of such perturbations.

#### 4 Conclusions

Numerical wave tanks have been constructed to study the effect of modulations in the propagation of regular waves in unidirectional seas through WCSPH simulations. Quantitative investigations have been carried out for the different parameters involved in these simulations to study their effect on the modulation mechanism. Further, the effect of water depth *d* has been also investigated in modification of the wave amplitude in such wave propagation scenarios. The results from this study can be utilized for the design of wave tank experiments and numerical simulations in future to study the phenomenon of modulational instability in oceanic environments. Such efforts can hopefully provide further meaningful insight into the mechanisms behind extreme energy localizations and rogue waves in oceans.

Numerical simulations of double focusing irregular waves have been used to validate the numerical model chosen for the study in addition to study of a Peregrine type breather evolution in our numerical wave tank. For the focusing of the double wave groups, considerable agreement is obtained between the numerical results and the experimental readings at small distances from the wavemaker, which has been illustrated through surface elevation and wavelet energy spectrum plots. A good qualitative agreement with respect to the focusing phenomenon is also found at locations further down

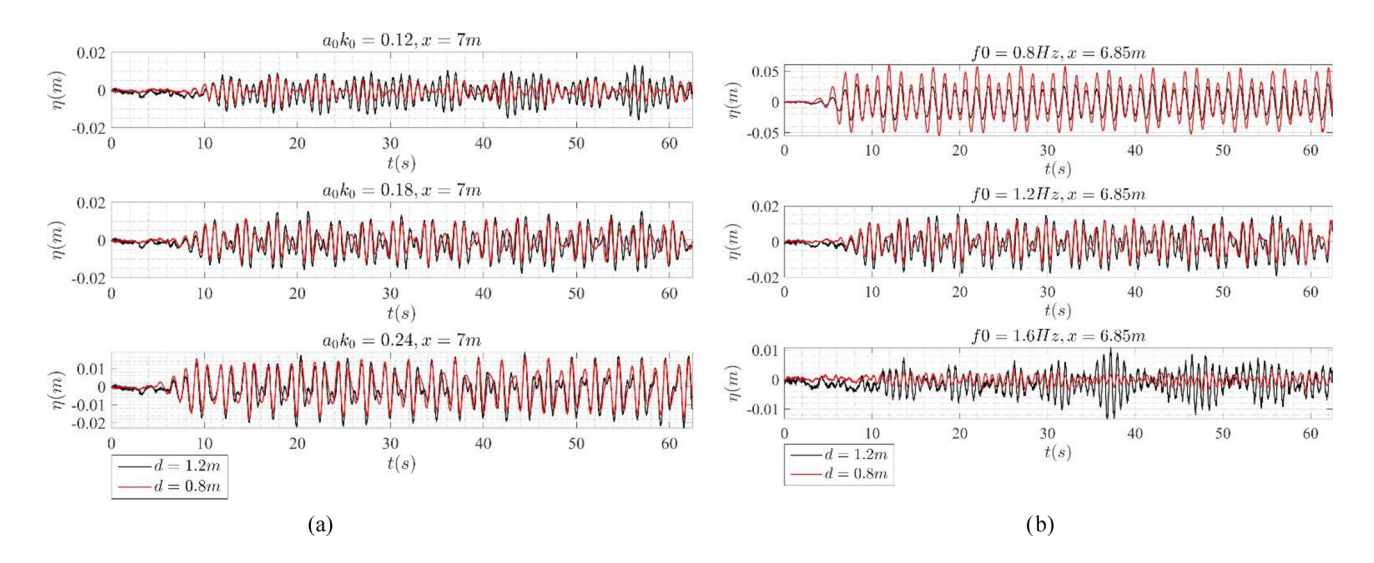


Fig. 20 a Surface elevation comparisons between d=1.2 m and d=0.8 m at x=7 m for  $\widetilde{a}_0k_0=0.12$ ,  $\widetilde{a}_0k_0=0.18$  and  $\widetilde{a}_0k_0=0.24$  (b) Surface elevation comparisons between d=1.2 m and d=0.8 m at x=6.85 m for  $f_0=0.8$  Hz,  $f_0=1.2$  Hz and  $f_0=1.6$ Hz



the numerical wave tank; however, the readings fall short of the experimental findings due to the inherent numerical dissipation of the chosen scheme. However, it must be kept in mind that any length of a numerical tank can be easily simulated through appropriate scaling, thus, allowing us for to make an informed judgement about required accuracy and allowed computational expense.

For the studies on the perturbed plane waves carried out using this setup, eigenvalue, frequency, and wavelet energy spectra are computed using the measured surface elevations to capture the effects of the different involved parameters. The sideband fraction  $(b_F)$  and the sideband imbalance  $(\alpha)$ , which determine the magnitude and the asymmetry of the sidebands respectively are found to have a significant effect on the wave evolution. Larger values of  $b_F$  result in larger wave amplitudes signifying the influence of the sidebands in such wave evolution scenarios. For  $\alpha$ , more negative values result in larger wave amplitudes. This observation, combined with the findings from  $b_F$  studies ascertain that the lower sideband in such scenarios play a more dominant role than the upper sideband in facilitating higher wave amplitudes over the NWT. The relative phase  $(\Phi)$  between the carrier band and the sidebands does not influence the wave evolution significantly according to this study. According to the investigations on the initial steepness  $(\tilde{a}_0 k_0)$ , the wave amplitude increases with increasing values of  $\tilde{a}_0 k_0$ , and the increase can be attributed to the growth of the smaller sideband. For carrier band frequencies  $(f_0)$ , smaller values result in larger wave amplitudes by virtue of the frequency dispersion relationship, however, the evolution cannot be attributed to the perturbation growth. The studies on modulational frequency  $(\Omega_M)$  revealed that increasing this parameter led to higher wave amplitudes due to sideband growth up to a certain threshold value. Increasing beyond this value does not result in higher wave amplitudes. The ratio of this threshold value to the carrier mode frequency is found out to be 4.167 in this case. The investigations on the effect of water depth d in this modulation process using the different parameters reveal that the impact of perturbations diminish with decreasing depth d, demonstrating that this modulational process is predominantly effective in deep sea waters.

As discussed above, the sideband fraction  $(b_F)$ , sideband imbalance  $(\alpha)$  and modulational frequency  $(\Omega_M)$  has a considerable influence on the behavior of plane modulated waves in a numerical wave tank. Qualitatively, it was found out that increase of  $b_F$  results in increased energy localization, however the rate of increase slows down progressively. For  $\alpha$ , the energy localization is dependent on both the sign and the magnitude of the parameter. The energy localization increases with increasing negative values of this parameter, as pointed above, implying the influence of the lower frequency sideband. However, to get a quantitative outlook into the nature of these parametric responses, a large number of experiments will need to be carried out in future. The

parameter  $\Omega_M$  also shows an increasing energy localization trend in the lower perturbation sideband with increasing values, however, only minor increase can be observed after a certain limit. This shows a non-linear response in regard to the ratio between the modulation frequency parameter  $\Omega_M$  and the carrier frequency  $f_0$  if energy localization is considered. This non-linear response characteristic will be quantified through numerical experiments in future.

These simulations, as mentioned previously, can easily be used for much larger scale scenarios through suitable scaling of the inter-particle distances and smoothing lengths. The results from these simulations can be used to design numerical wave tank experiments to study different kinds of rapid wave formations in oceanic environments. The observations from this study can serve as a foundation for pursuing further numerical investigations into the mechanism of modulational instability leading to rogue wave events in oceans. These numerical simulations can also pave the way for looking at other mechanisms of extreme oceanic wave formations listed in §1. The authors intend to extend the 2-D simulations into 3 dimensions in future endeavors using improved GPU parallelization techniques for a more realistic outlook into such energy localization scenarios. It is hoped that the results acquired from such studies, blended with improved deep learning techniques can significantly aid in the prediction of such extreme oceanic events in future. Furthermore, as has been observed during our validation studies and investigations using the plane perturbed waves, numerical dissipative effects can hinder the full evolution of small amplitude waves at large distances from the wavemaker in WCSPH models. The authors intend to investigate the effect of numerical dissipation in such scenarios in greater detail in future efforts.

#### **Appendix**

Evolution of Peregrine-type breather in NWT using WCSPH

The Non-linear Schrödinger equation is the simplest theoretical model to explain the evolution of a unidirectional and narrow-banded modulated wave group in deep water, which can result in the formation of steep ocean waves through modulational instability. This equation admits a number of breather type soliton solutions. The Peregrine breather is one such soliton which is localized in both space and time, and the soliton breathes only once during its motion. The modulation evolution of the Peregrine breather solution has been investigated through wave tank simulations here.

Using the notations described in Shemer and Alperovich [34], the water surface elevation  $\zeta(x, t)$  for a wave group with carrier frequency  $\omega_0$  and wavenumber  $k_0$  satisfying the frequency dispersion relationship is given by:



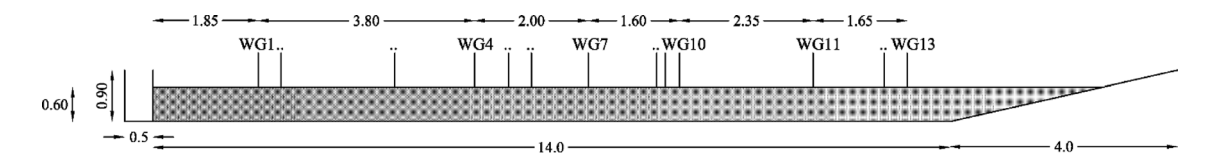
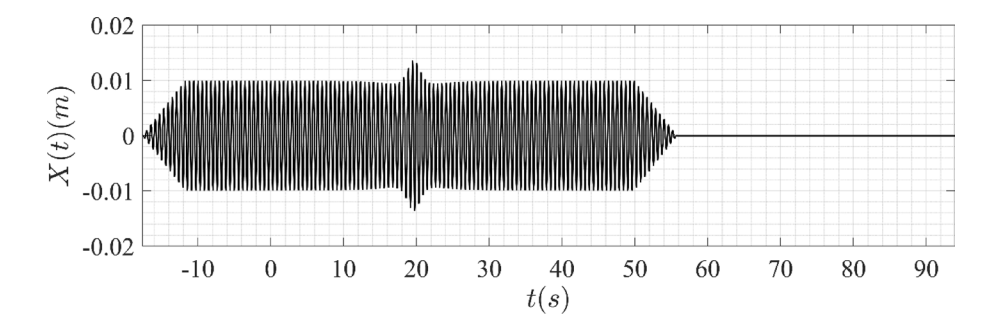
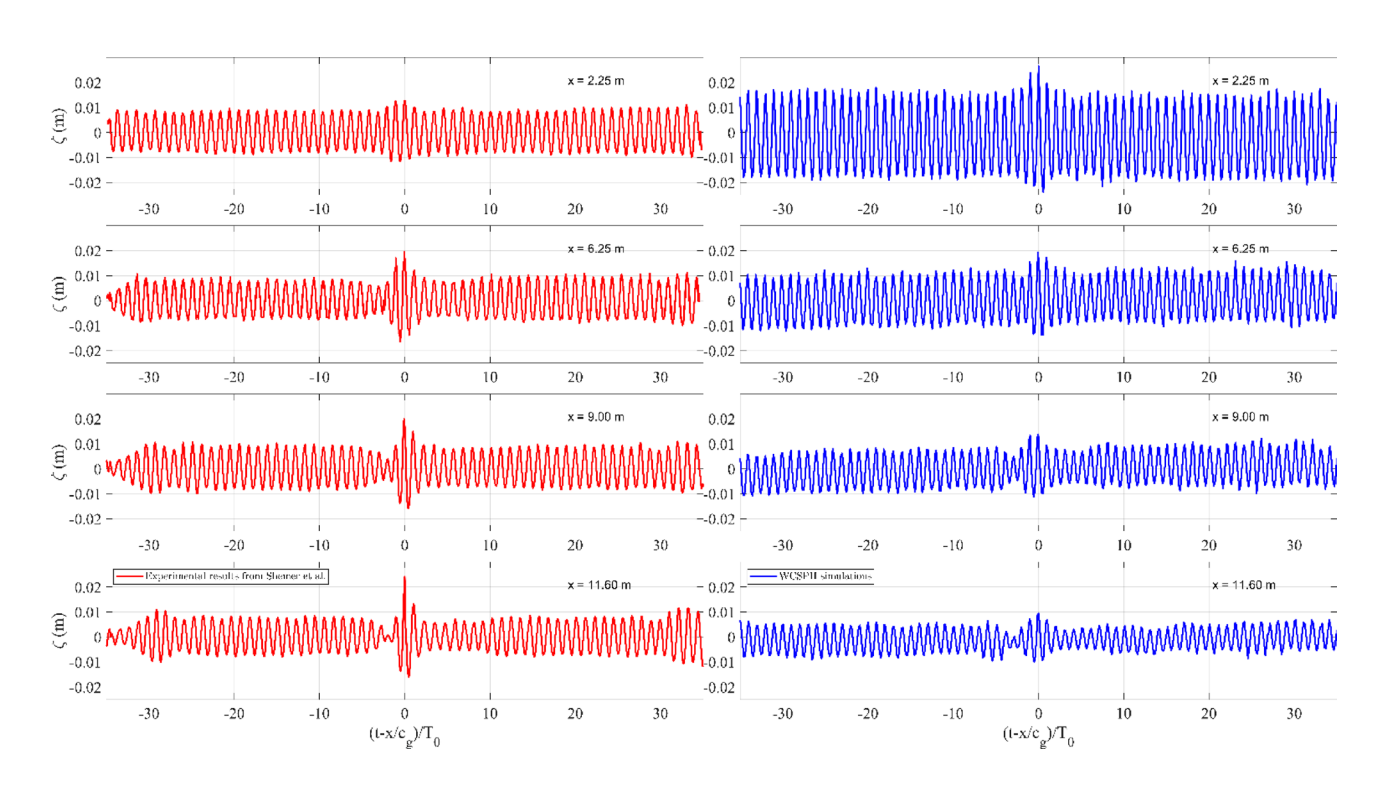


Fig. 21 Numerical setup for Peregrine-type wave experiments. All dimensions are provided in meters. 13 wave gauges have been used for these simulations and located as shown in the figure. These are depicted using WGs

**Fig. 22** The motion imparted by the flap wavemaker at x = 0 m. The maximum amplitude of the Peregrine breather is set at  $X_0 = 9$  m. The proportionality factor is taken to be  $\alpha = 1$ . The flap motion is kept at 0 for 65  $T_0$  after the tapered motion at the end to capture the observations at farther locations from the wavemaker





**Fig. 23** The evolution of a modulated wave group in a wave tank studied through surface elevation readings at different locations. The left plot shows the results from experiments carried out by Shemer

et al. [34] The right plot shows the results from the WCSPH simulations in the present study

$$\zeta(x,t) = Re\left[a(x,t) e^{i\left(k_0 x - \omega_0 t\right)}\right] \tag{29}$$

where a(x, t) is the slowly varying complex wave group envelope. The characteristic wave amplitude  $a_0$ , the wave

steepness  $\varepsilon = a_0 k_0$  and the wave group velocity  $c_g$  are used to give the spatial NLS equation as

$$-i\frac{dA}{d\eta} + \frac{\partial^2 A}{\partial \xi^2} + |A|^2 A = 0 \tag{30}$$



where 
$$\xi = \varepsilon \omega_0 \left(\frac{x}{c_o} - t\right); \eta = \varepsilon^2 k_0 x; A(\xi, \eta) = a/a_0$$

The Peregrine soliton written in terms of these dimensionless variables is given by

$$A(\xi,\eta) = -\sqrt{2} \left[ 1 - \frac{4(1 - 4i\eta)}{1 + 4\xi^2 + 16\eta^2} \right] e^{-2i\eta}$$
 (31)

The experiments detailed out in Shemer and Alperovich [34] were carried out in a wave tank 18 m long, 1.2 m wide and 0.9 m deep with a programmable flap type wave-maker for wave generation. The simulations in the present study are carried out in a 2D numerical wave tank which is 18.5 m long and 0.9 m deep, with a slope at the end starting from 14 m for passive wave absorption to reduce wave reflection. A flap type wavemaker at x = 0m is used for the wave generation. Surface elevation measurements were obtained at 13 different locations along the wave tank, as depicted in the simulation setup is provided in Fig. 21.

Simulations have been carried out using a water depth of d=0.6 m with the parameters: period  $T_0=0.587s$ , corresponding to  $k_0=0.587s$ ,  $\lambda_0=0.538m$ ,  $\varepsilon=0.0825$  and

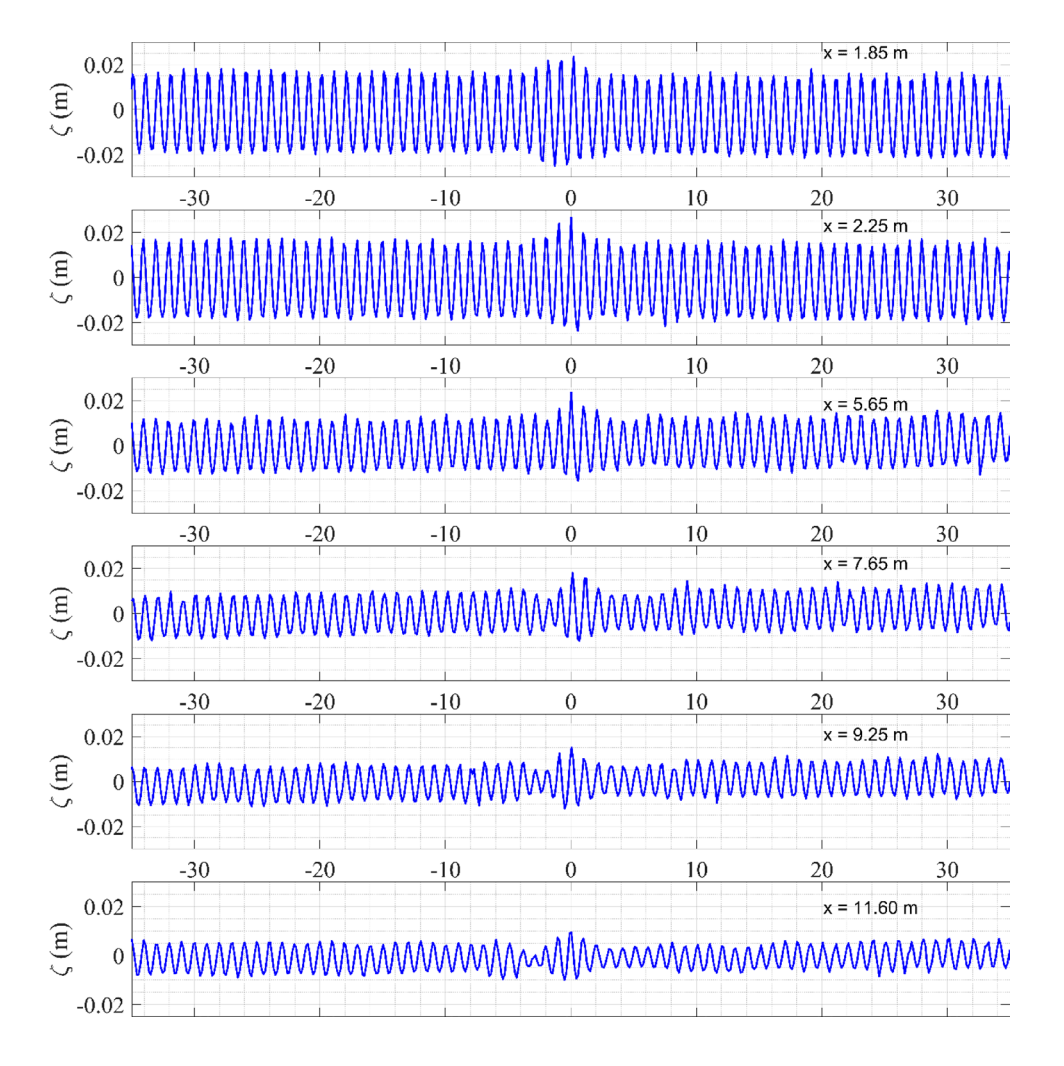
 $\zeta_0 = 0.01m$ . The flap wavemaker motion is calculated using the Eqs. 29, 30 and 31 with a proportionality factor to achieve the wavemaker motion as

$$X(t) = \alpha A(x, t) \tag{32}$$

where  $\alpha$  is the proportionality factor utilized to achieve a certain surface elevation during the wave tank simulations. The A(x,t) in Eq. 32 [34] is computed to achieve the maximum of the Peregrine soliton at  $X_0 = 9m$ . The total duration of the wave group itself has been taken to be  $115T_0$  with tapering windows of  $10T_0$  over the two end periods. The wavemaker motion for  $\alpha = 1$  is given in Fig. 22.

The surface elevation readings at 4 different locations given in Shemer and Alperovich [34] are used to look at the evolution of the modulation along the wave tank. Considering the numerical dissipation present in WCSPH models, a proportionality factor of  $\alpha = 1.5$  was used during the wave generation to obtain a background wave amplitude at  $X_0 = 9m$ , similar to that observed in the experimental results detailed in Shemer and Alperovich [34]. The simulation

**Fig. 24** The evolution of the modulated wave group in the numerical wave tank using a flap type wavemaker with  $\alpha = 1.5$ . Surface elevation readings at six different locations are depicted with respect to the wave group velocity. The center of the modulated wave group is at  $(t - x/c_g)T_0 = 0$ 





observations along with the experimental results given in [34] are depicted in Fig 23.

From the surface elevation plots in Fig. 23, it can be observed that there are significant differences between the experimental results in Shemer and Alperovich [34] and the observations using the WCSPH simulations. This can be attributed to the numerical dissipation present in WCSPH. This results in gradual decrease of the background wave amplitude with increasing distance from the wavemaker at x = 0m. The evolution of the modulation can be observed

clearly in the experimental results from the left plot with the maximum modulation amplitude observed at x = 11.6m. To get a better picture of the modulation evolution in our simulations, the surface elevation observations at more locations along the wave tank are depicted in Fig. 24. The surface elevation observations for the WCSPH simulations at six different locations along the numerical tank are shown in Fig. 24. It can be seen from these plots that the background wave amplitude gradually starts to decrease with increasing

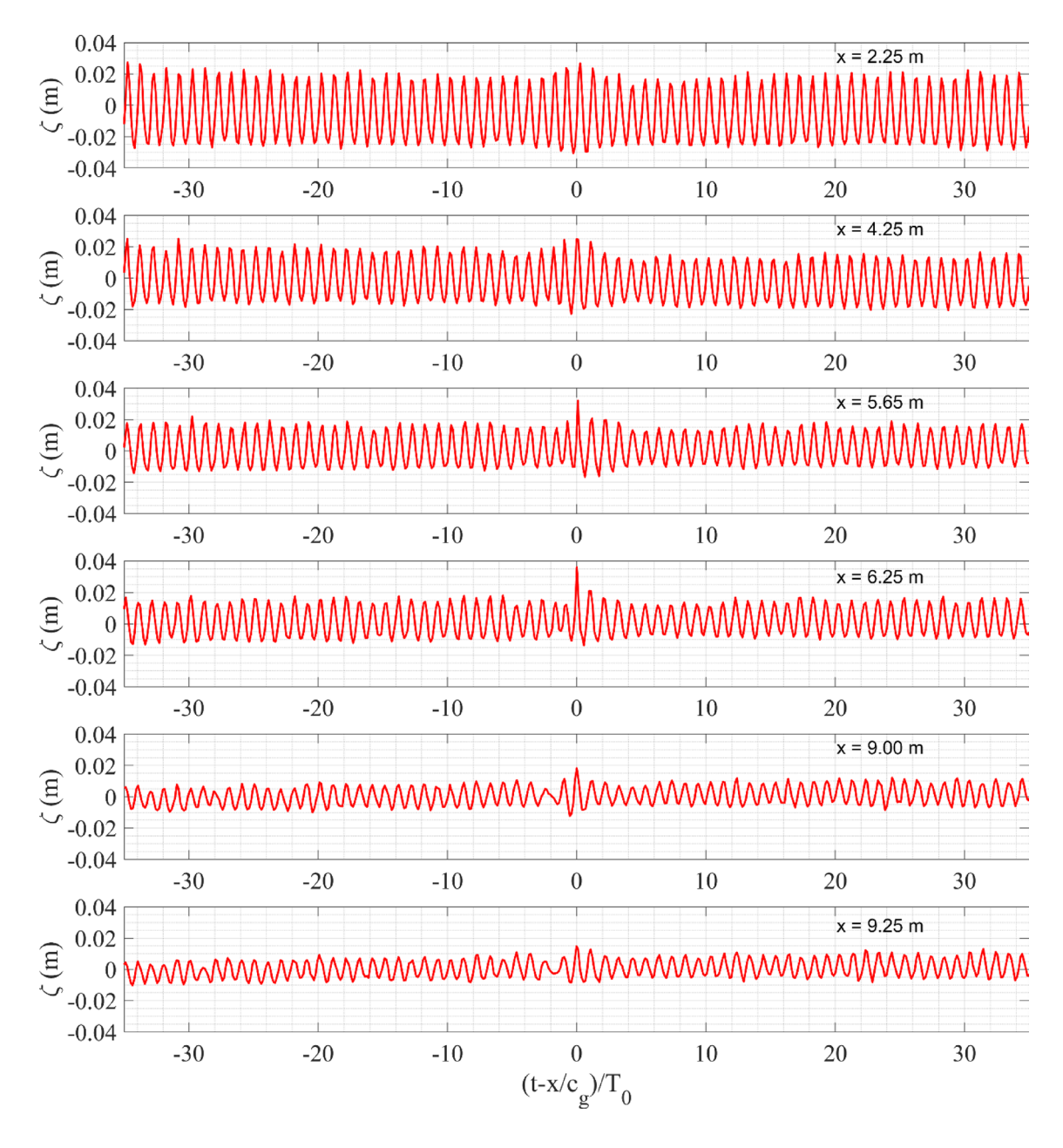


Fig. 25 The evolution of the modulated wave group in the numerical wave tank using a flap type wavemaker with  $\alpha = 3.0$ . Surface elevation readings at six different locations are depicted with respect to the wave group velocity. The center of the modulated wave group is at  $(t - x/c_g)T_0 = 0$ 



distance from the wavemaker due to numerical dissipative effects.

However, the growth of the modulation can be observed clearly by looking at the ratio of the peak modulation amplitude to the average background wave amplitude. For the sake of subsequent break-down of the observations, this will be referred to as the amplitude ratio  $\chi$  in further discussions. At x = 1.85m, the ratio  $\gamma$  is observed to be 1.31. The growth of the modulation down the numerical wave tank can be observed from the plots at x = 2.25m and x = 5.65m. The amplitude ratio  $\chi$  is found to increase to 1.49 at x = 2.25m and 1.92 at x = 5.65m, where it is found to reach the maximum during the simulation duration. The modulation amplitude starts diminishing after this position, with the amplitude ratio between the modulation and the background going down to 1.8 and 1.5 at x = 7.65m and x = 11.6m respectively. These observations depict the evolution of a modulated wave group for a Peregrine-type breather solution for NLSE in our developed NWT. However, due to the numerical dissipation in the WCSPH model, the amplitude, and the location of the maximum evolution amplitude in the simulation results differ from theoretical and experimental results given in Shemer and Alperovich [34].

A second set of simulations was performed using a larger proportionality factor of  $\alpha = 3.0$  using the same set of parameters. Wave breaking is not observed during the course of this simulation. The surface elevation readings at six separate locations for these simulations are given in Fig. 25. Similar to the case of  $\alpha = 1.5$ , it is observed from the plots in Fig. 25 that the background wave amplitude decreases with increasing distance from the wavemaker. However, the ratio of the modulation amplitude to the background amplitude shows a growth from x = 0m to x = 6.25m. As observed from the elevation readings in Fig. 25, the amplitude ratio  $\chi$  shows an increase from the initial ratio of 1.3 at the wavemaker to  $\chi = 1.35$  at x = 2.25m. The modulation gets enhanced further down the numerical wave tank as observed from the plots at x = 4.25m, x = 5.65m and x = 6.25m. The amplitude ratio  $\chi$  evolves through 1.47 and 2.125 at x = 4.25m and x = 5.65m respectively to a maximum of  $\chi = 2.8$  at x = 6.25m. Similar to the case of  $\alpha = 1.5$ , the amplitude ratio is observed to reduce after this location, with the values observed being 1.8 and 1.66 at x = 9m and x = 9.25m respectively. The numerical experiments carried out for the Peregrine-type breather extend our validation efforts for the numerical WCSPH scheme utilized in our studies of plane modulated waves. It can be ascertained from these simulation results that the developed numerical scheme is able to capture the modulation evolution process that results in the formation of large Peregrine type breather solutions to the NLSE, which is very similar to observed extreme waves in oceans. However, there are discernible differences when compared to previous experimental studies

on these waves. Such disagreements can be attributed to the numerical dissipation which is necessary for the stability of the weakly compressible scheme in our studies. This mainly gets manifested for waves with smaller amplitudes and larger distances from the wavemaker. Thus, for the larger proportionality factor that we have used in our study, the modulation growth was observed to be more prominent. The phenomenon of numerical dissipation in our model and methods to reduce its effects will be investigated in future studies to be carried out by the authors.

**Acknowledgements** Support received for this work through U.S. National Science Foundation Grant No. CMMI1854532 is gratefully acknowledged. The authors are also grateful for the high speedup that HPC resources of the MARCC computing cluster allowed in this study.

Author contributions Conceptualization: BB, KI, and SC; numerical experiments and investigations: SC; writing—original draft preparation: SC and BB; writing—review and editing: KI, BB, and SC; supervision: BB and KI funding acquisition: BB All authors have read and agreed to this version of the manuscript.

**Funding** This research was funded by through U.S. National Science Foundation grant no. CMMI1854532.

**Data availability statement** Data generated through the simulations are available through the manuscript and/or from the authors.

#### **Declarations**

**Conflict of interest** The authors declare no conflict of interest.

# References

- Adcock TAA, Taylor PH, Yan S, Ma QW, Janssen PAEM (2011) Did the Draupner wave occur in a crossing sea? Proc. R. Soc. Math. Phys. Eng. Sci. 467:3004–3021. https://doi.org/10.1098/ rspa 2011 0049
- Adcock TAA, Taylor PH (2014) The physics of anomalous ('rogue') ocean waves. Rep Prog Phys. https://doi.org/10.1088/ 0034-4885/77/10/105901
- Akhmediev N, Ankiewicz A, Taki M (2009) Waves that appear from nowhere and disappear without a trace. Phys Lett A 373:675–678. https://doi.org/10.1016/j.physleta.2008.12.036
- Altomare C, Domínguez JM, Crespo AJC, González-Cao J, Suzuki T, Gómez-Gesteira M, Troch P (2017) Long-crested wave generation and absorption for SPH-based DualSPHysics model. Coast Eng 127:37–54. https://doi.org/10.1016/j.coastaleng.2017.06.004
- Antuono M, Colagrossi A, Marrone S, Molteni D (2010) Freesurface flows solved by means of SPH schemes with numerical diffusive terms. Comput Phys Commun 181:532–549. https://doi. org/10.1016/j.cpc.2009.11.002
- Barratt, M., 2016. What conditions led to the Draupner freak wave? [WWW Document]. ECMWF. URL https://www.ecmwf. int/en/newsletter/148/meteorology/what-conditions-led-draupner-freak-wave (accessed 2.19.23).
- Batchelor CK, Batchelor GK (1967) An Introduction to Fluid Dynamics. Cambridge University Press
- Biésel F, Suquet F (1951) Laboratory wave generating apparatus. Houille Blanche 37:147–165. https://doi.org/10.1051/lhb/19510
   33



- Bluecrab HPC Cluster [WWW Document], n.d. UMD High Perform. Comput. URL http://hpcc.umd.edu//hpcc/bluecrab.html (Accessed 2.19.23).
- Bonnefoy F, Tikan A, Copie F, Suret P, Ducrozet G, Pradehusai G, Michel G, Cazaubiel A, Falcon E, El G, Randoux S (2020) From modulational instability to focusing dam breaks in water waves. Phys Rev Fluids. https://doi.org/10.1103/PhysRevFluids.5.034802
- Chabalko C, Moitra A, Balachandran B (2014) Rogue waves: new forms enabled by GPU computing. Phys Lett A 378:2377–2381. https://doi.org/10.1016/j.physleta.2014.06.013
- Chakraborty S, Balachandran B (2021) Wave propagation studies in numerical wave tanks with weakly compressible smoothed particle hydrodynamics. J Mar Sci Eng. https://doi.org/10.3390/jmse9020233
- Chalikov D (2007) Numerical simulation of the Benjamin-Feir instability and its consequences. Phys Fluids 19:16602. https:// doi.org/10.1063/1.2432303
- Dehnen W, Aly H (2012) Improving convergence in smoothed particle hydrodynamics simulations without pairing instability. Mon Not R Astron Soc 425:1068–1082. https://doi.org/10.1111/j. 1365-2966.2012.21439.x
- Diego M, Colagrossi A (2009) A simple procedure to improve the pressure evaluation in hydrodynamic context using the SPH. Comput Phys Commun 180:861–872. https://doi.org/10.1016/j. cpc.2008.12.004
- Eeltink D, Branger H, Luneau C, He Y, Chabchoub A, Kasparian J, van den Bremer TS, Sapsis TP (2022) Nonlinear wave evolution with data-driven breaking. Nat Commun 13:2343. https://doi.org/ 10.1038/s41467-022-30025-z
- Gemmrich J, Cicon L (2022) Generation mechanism and prediction of an observed extreme rogue wave. Sci Rep 12:1718. https://doi.org/10.1038/s41598-022-05671-4
- Helal MA, Seadawy AR (2012) Benjamin-Feir instability in nonlinear dispersive waves. Comput Math Appl 64:3557–3568. https://doi.org/10.1016/j.camwa.2012.09.006
- Karpman VI, Lynov JP, Michelsen PK, Juul Rasmussen J (1996) Modulational instability of plasma waves in two dimensions. Math Comput Simul 40:223–234. https://doi.org/10.1016/0378-4754(95)00034-8
- Kharif, C., Pelinovsky, E., Slunyaev, A., 2008. Rogue Waves in the Ocean. Springer Science and Business Media.
- Kumar NK, Savitha R, Al Mamun A (2018) Ocean wave height prediction using ensemble of Extreme Learning Machine. Neurocomputing, Hierarchical Extreme Learning Machines 277:12–20. https://doi.org/10.1016/j.neucom.2017.03.092
- Lind SJ, Xu R, Stansby PK, Rogers BD (2012) Incompressible smoothed particle hydrodynamics for free-surface flows: A generalised diffusion-based algorithm for stability and validations for impulsive flows and propagating waves. J Comput Phys 231:1499– 1523. https://doi.org/10.1016/j.jcp.2011.10.027
- Manolidis M, Orzech M, Simeonov J (2019) Rogue Wave Formation in Adverse Ocean Current Gradients. J Mar Sci Eng 7:26. https://doi.org/10.3390/jmse7020026
- MATLAB MathWorks [WWW Document], n.d. URL https:// www.mathworks.com/products/matlab.html (Accessed 6.14.22).
- Modulational Instability and Rogue Waves in Crossing Sea States in: Journal of Physical Oceanography Volume 48 Issue 6 (2018)

- [WWW Document], n.d. URL https://journals.ametsoc.org/view/journals/phoc/48/6/jpo-d-18-0006.1.xml?tab\_body=fulltext-displ ay (Accessed 3.2.21).
- Moitra A, Chabalko C, Balachandran B (2016) Extreme wave solutions: Parametric studies and wavelet analysis. Int J Non-Linear Mech 83:39–47. https://doi.org/10.1016/j.ijnonlinmec.2016. 03.011
- Monaghan JJ (2012) Smoothed particle hydrodynamics and Its diverse applications. Annu Rev Fluid Mech 44:323–346. https:// doi.org/10.1146/annurev-fluid-120710-101220
- Monaghan JJ (1992) Smoothed Particle Hydrodynamics. Annu Rev Astron Astrophys 30:543–574. https://doi.org/10.1146/annur ev.aa.30.090192.002551
- Morlet wavelet MATLAB morlet [WWW Document], n.d. URL https://www.mathworks.com/help/wavelet/ref/morlet.html (Accessed 6.14.22).
- Morris JP, Fox PJ, Zhu Y (1997) Modeling low reynolds number incompressible flows using SPH. J Comput Phys 136:214–226. https://doi.org/10.1006/jcph.1997.5776
- NVIDIA CUDA Toolkit Release Notes [WWW Document], n.d. URL https://docs.nvidia.com/cuda/cuda-toolkit-release-notes/ index.html (Accessed 6.14.22).
- Onorato M, Osborne AR, Serio M (2006) Modulational instability in crossing sea states: a possible mechanism for the formation of freak waves. Phys Rev Lett. https://doi.org/10.1103/PhysRevLett. 96.014503
- Pelinovsky, E., Kharif, C., 2008. Extreme Ocean Waves. Springer Science and Business Media.
- Shemer L, Alperovich L (2013) Peregrine breather revisited. Phys Fluids DOI. https://doi.org/10.1063/1.4807055
- Wang L, Li JX, Liu, SX, Fan YP, 2020. Experimental and Numerical Studies on the Focused Waves Generated by Double Wave Groups. Front. Energy Res. 8.
- Wang R, Balachandran B (2018) Extreme wave formation in unidirectional sea due to stochastic wave phase dynamics. Phys Lett A 382:1864–1872. https://doi.org/10.1016/j.physleta.2018.04.050
- Zakharov VE, Shabat AB (1972) Exact Theory of Two-dimensional Self-focusing and One-dimensional Self-modulation of Waves in Nonlinear Media. Sov J Exp Theor Phys 34:62
- Zaratan HPC Cluster, UMD High Performance Computing. http:// hpcc.umd.edu//hpcc/zaratan.html. Accessed 21 Sep 2023
- Zou, Q., Chen, H., 2017. Wind and Current Effects on Extreme Wave Formation and Breaking. https://doi.org/10.1175/ JPO-D-16-0183.1

**Publisher's Note** Springer Nature remains neutral with regard to jurisdictional claims in published maps and institutional affiliations.

Springer Nature or its licensor (e.g. a society or other partner) holds exclusive rights to this article under a publishing agreement with the author(s) or other rightsholder(s); author self-archiving of the accepted manuscript version of this article is solely governed by the terms of such publishing agreement and applicable law.

